

**Dictionary Learning and Low-rank Sparse Matrix Decomposition for
Sparsity-driven SAR Image Reconstruction**

by
Abdurrahim Soğanlı

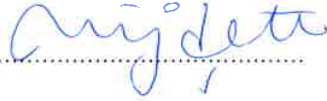
Submitted to the Graduate School of Engineering and Natural Sciences
in partial fulfillment of
the requirements for the degree of
Master of Science

Sabancı University
September 2014

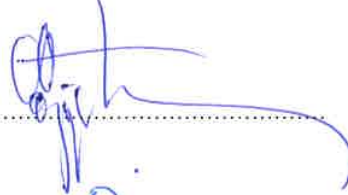
Dictionary Learning and Low-rank Sparse Matrix Decomposition for Sparsity-driven
SAR Image Reconstruction

APPROVED BY

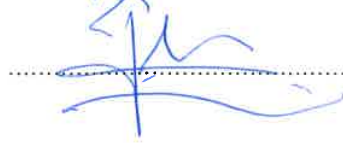
Assoc. Prof. Dr. Müjdat ÇETİN
(Thesis Supervisor)



Assoc. Prof. Dr. Özgür Erçetin



Prof. Dr. S. İlker Birbil



DATE OF APPROVAL: 10/09/2014

© Abdurrahim Sođanlı 2014
All Rights Reserved

to my family

Acknowledgments

I must say that I am proud of having done my undergraduate and graduate degree from Sabancı University.

I would like to express my sincere appreciation to my advisor Müjdat Çetin for his valuable support throughout the three years of my studies. When I was a junior during my undergraduate studies, he spared time for me and trusted me. Undoubtedly I would not have been able to write this thesis without his support and motivation.

I would like to specially thank Özgür Erçetin for his valuable guidance during my graduate studies. I am grateful to him for his professional and academic advice. I also would like to thank İlker Birbil for participating in my thesis committee. I am very thankful to all my friends in VPA lab. I would like to give a special thanks to former VPA lab member Özben Önhon for her advice and support during my study.

This work was partially supported by the Scientific and Technological Research Council of Turkey (TUBITAK) through a graduate fellowship. I would like to thank TUBITAK-BIDEB for providing financial support for my graduate education.

I would also like to thank Efe Öztürk, Enes Şafak, Mustafa Hakköz, and Buğra Demirkol for their valuable friendship.

Finally but most importantly, I would like to thank my parents Selim and Gülten, and my sisters for their support and for trusting me throughout my life.

Dictionary Learning and Low-rank Sparse Matrix Decomposition for Sparsity-driven SAR Image Reconstruction

Abdurrahim Soğanlı

EE, M.Sc. Thesis, 2014

Thesis Supervisor: Müjdat Çetin

Keywords: Synthetic aperture radar (SAR), image reconstruction, dictionary learning, sparse representation, low-rank sparse matrix decomposition

Abstract

Synthetic aperture radar (SAR) is one of the most widely used remote sensing modalities, providing images for a variety of applications including those in defense, environmental science, and weather forecasting. However, conventionally formed SAR imagery from undersampled observed data, arising in several emerging applications and sensing scenarios, suffers from artifacts that might limit effective use of such imagery in remote sensing applications. Recently, sparsity-driven SAR imaging has emerged as an effective framework to alleviate such problems. Sparsity-based methods for SAR imaging have employed overcomplete dictionaries to represent the magnitude of the complex-valued field sparsely. Selection of an appropriate dictionary with respect to the features of the particular type of underlying scene plays an important role in these methods.

In this thesis, we develop two new sparsity-driven SAR imaging methods that significantly expand the domain of applicability of sparsity-based methods in SAR imaging. Our first contribution involves the development of a new reconstruction method that is based on learning sparsifying dictionaries and using such learned dictionaries in the reconstruction process. Adaptive dictionaries learned from data can represent the mag-

nititude of complex-valued field more effectively and hence have the potential to widen the applicability of sparsity-based radar imaging. Our framework allows the use of both adaptive dictionaries learned offline from a training set and those learned online from the undersampled data used in image formation. We demonstrate the effectiveness of the proposed dictionary learning-based SAR imaging approach as well as the improvements it provides, on both synthetic and real data.

The second contribution of this thesis involves the development of a reconstruction method that decomposes the imaged field into a sparse and a low-rank component. Such a decomposition is of interest in image analysis tasks such as segmentation and background subtraction. Conventionally, such operations are performed after SAR image formation. We exploit recent work on sparse and low-rank decomposition of matrices and incorporate such a decomposition into the process of SAR image formation. The outcome is a method that jointly reconstructs a SAR image and decomposes the formed image into its low-rank background and spatially sparse components. We demonstrate the effectiveness of the proposed method on both synthetic and real SAR images.

Dictionary Learning and Low-rank Sparse Matrix Decomposition for Sparsity-driven
SAR Image Reconstruction

Seyreklik Gdml SAR Geriatımı iin Szlk ğrenimi ve Dşk Sıralı Seyrek
Matris Ayrışımı

Abdurrahim Soğanlı

EE, Yksek Lisans Tezi, 2014

Tez Danışmanı: Mjdat etin

Anahtar Kelimeler: Sentetik aıklıklı radar (SAR), imge geriatımı, szlk
ğrenimi, seyreklik temsili, dşk sıralı seyrek matris ayrışımı

zet

Sentetik aıklıklı radar (SAR) savunma, evre bilimi ve hava tahmini gibi eşitli uygulamalarda sıklıkla kullanılan uzaktan algılama yntemlerinden biridir. Ancak verinin dşk rneklemeye gzlemlendiği durumlarda geleneksel yntemler ile elde edilmiş SAR grntleri yapay dokulara neden olmakta ve bu durum SAR grntlerinin uzaktan algılama yntemlerinde etkili kullanımına engel olmaktadır. Son zamanlarda bu sorunları azaltmak iin seyreklik tabanlı SAR grntleme ortaya ıkmıştır. Seyreklik tabanlı yntemler karmaşık değeri yapının mutlak değeri seyrek bir şekilde temsil edebilmek iin szlk kullanırlar. Bu yntemlerde grntnn zelliklerine gore uygun bir szlğn seilmesi ok nemlidir.

Bu tezde seyreklik tabanlı yntemlerin daha geniş bir biimde SAR grntlerine uygulanmasını saėlayacak iki yeni seyreklik tabanlı SAR grntleme yntemi neriyoruz. Birinci katkı olarak seyreklik szlğnn ğrenilmesine dayanan ve bu ğrenilen szlğ SAR grntlerinin geri atılma işleminde kullanılmasını saėlayan bir yntem geliştiriyoruz. Verinin kendisinden ğrenilen uyarlanırlar szlklerin karmaşık değeri

yapımın mutlak deęerini daha etkili bir şekilde temsil etme potensiyelleri vardır ve ve bu sözlükler seyreklik tabanlı görüntülemeyi daha geniş bir biçimde uygulanmasını sağlar. Bu önerdiğimiz yöntem uyarlanır sözlüklerin bir eğitim kümesinden çevirimdışı olarak öğrenilmesini sağlayabildiği gibi sözlüğün hedef verinin kendisinden çevirimiçi şekilde öğrenilmesini de sağlamaktadır. Önerdiğimiz sözlük öğrenimi tabanlı SAR görüntüleme yönteminin etki ve katkısını sentetik ve gerçek SAR görüntülerinde gösteriyoruz.

Bu tezdeki ikinci katkı olarak görüntüyü seyrek ve düşük sıralı bileşenlerine ayıran bir geri çatma yöntemi öneriyoruz. Bu ayırma yöntemi bölütleme ve arkaplan çıkarımı gibi birçok görüntü tahlil yönteminde ilgi çekmektedir. Geleneksel olarak bu görüntü tahlil yöntemleri SAR görüntüsünün oluşturulmasından sonra yapılır. Biz yeni bir çalışma olan seyrek ve düşük sıralı matrislerin ayrıştırılması yöntemini SAR görüntüleme işleminde kullanıyoruz. Sonuç olarak SAR görüntüsünü geri çatarken aynı zamanda görüntüdeki seyrek bileşenleri ve düşük sıralı arkaplanı da ayırmaktayız. önerdiğimiz yöntemin etkisini sentetik ve gerçek SAR görüntülerinde gösteriyoruz.

Table of Contents

Acknowledgments	v
Abstract	vi
Özet	viii
1 Introduction	1
1.1 Problem Definition and Motivation	1
1.2 Contributions of this Thesis	4
1.3 Organization of the Thesis	5
2 Background	6
2.1 Synthetic Aperture Radar Basics	6
2.1.1 Principles of SAR Imaging	6
2.1.2 Spotlight-mode SAR Signal Model	9
2.2 Image Reconstruction and Sparse Representation	10
2.2.1 Regularization in Image Processing	11
2.2.2 Sparse Representation	13
2.2.3 Compressed Sensing	14
2.3 Dictionary Learning	15
2.3.1 K-SVD	16
2.4 SAR Image Reconstruction Methods	19
2.4.1 Conventional Methods	19
2.4.2 Sparsity-driven SAR Image Reconstruction Methods	19
2.4.3 Recent SAR Image Reconstruction Methods	22
2.5 Low-rank Matrix Recovery	22
2.5.1 Theoretical Background	22
2.5.2 Singular Value Thresholding (SVT)	24
2.5.3 Alternating Direction Method of Multipliers (ADMM)	24
2.5.4 Low-rank Sparse Decomposition (LRSD)	26

3	Dictionary Learning for Sparsity-Driven SAR Imaging	28
3.1	Proposed Dictionary Learning Framework	28
3.1.1	Sparse Coefficients and Dictionary Update	30
3.1.2	Phase Update Step	31
3.1.3	Magnitude Update Step	32
3.2	Experimental Results	33
3.2.1	Synthetic Scene Experiments	37
3.2.2	Real SAR Scene Experiments	43
4	Low-rank Sparse Decomposition Framework for SAR Imag-	
	ing	53
4.1	Proposed LRSD-based Framework	53
4.2	Solution of the Optimization Problem	56
4.3	Experimental Results	60
4.3.1	Synthetic Scene Experiments	60
4.3.2	Real SAR Scene Experiments	63
5	Conclusion and Future Work	69
5.1	Conclusion	69
5.2	Potential Future Directions	70

List of Figures

1.1	SAR data collection geometry. (Image obtained from the web site of Sandia National Laboratories.)	2
1.2	Arasen stadium, Norway. (a) Google Earth. (b) Conventionally reconstructed SAR image.	3
2.1	Ground-plane geometry for spotlight-mode SAR.	8
2.2	Graphical representation of the support of the known phase history data samples in 2D spatial frequency domain.	9
3.1	Graphical representation of the iterative algorithm.	31
3.2	Randomly selected 1000 training patches for offline dictionary learning based on synthetic scenes.	37
3.3	Offline learned 64×441 overcomplete dictionary.	38
3.4	Overcomplete 64×441 Haar dictionary.	38
3.5	Results of the synthetic experiment with available data ratio $L = 0.9$. (a) Original scene. (b) Conventional reconstruction. (c) Sparsity-driven point-region enhanced reconstruction. (d) Sparsity-driven reconstruction with overcomplete Haar dictionary. (e) Proposed method with offline dictionary learning. (f) Proposed method with online dictionary learning.	40
3.6	Results of the synthetic experiment with available data ratio $L = 0.8$. (a) Original scene. (b) Conventional reconstruction. (c) Sparsity-driven point-region enhanced reconstruction. (d) Sparsity-driven reconstruction with overcomplete Haar dictionary. (e) Proposed method with offline dictionary learning. (f) Proposed method with online dictionary learning.	41

3.7	Results of the synthetic experiment with available data ratio $L = 0.7$. (a) Original scene. (b) Conventional reconstruction. (c) Sparsity-driven point-region enhanced reconstruction. (d) Sparsity-driven reconstruction with overcomplete Haar dictionary. (e) Proposed method with offline dictionary learning. (f) Proposed method with online dictionary learning.	42
3.8	Online learned dictionaries for the synthetic test image with different L . (a) $L = 0.9$. (b) $L = 0.8$. (c) $L = 0.7$.	43
3.9	5 synthetic test images used for the quantitative analysis.	44
3.10	Results of the synthetic experiment with 5 test images. Different available data ratio values L vs MSE (a) Standard deviation of noise $\sigma = 0.01$. (b) $\sigma = 1$.	45
3.11	Training SAR images.	46
3.12	Learned dictionary from SAR images.	47
3.13	Result of inpainting of the SAR image with 50% missing pixels. (a) Original SAR scene. (b) %50 pixel missing data. (c) Inpainting result with overcomplete DCT. MSE = 0.0002547 (d) Inpainting result with learned dictionary. MSE = 0.0001666	48
3.14	Result of the first experiment with $L \approx 0.8$. (a) Reconstructed image with full data. (b) Zoomed in version of a part of a. (c) Conventional reconstruction. (d) Zoomed in version of a part of c. (e) Image reconstructed with point-region enhanced regularization. (f) Zoomed in version of a part of e. (g) Image reconstructed with overcomplete DCT. (h) Zoomed in version of a part of g. (i) Image reconstructed with offline learning. (j) Zoomed in version of a part of i. (k) Image reconstructed with online learning. (l) Zoomed in version of a part of k.	49

3.15	Result of the second experiment with $L \approx 0.7$. (a) Reconstructed image with full data. (b) Zoomed in version of a part of a. (c) Conventional reconstruction. (d) Zoomed in version of a part of c. (e) Image reconstructed with point-region enhanced regularization. (f) Zoomed in version of a part of e. (g) Image reconstructed with overcomplete DCT. (h) Zoomed in version of a part of g. (i) Image reconstructed with offline learning. (j) Zoomed in version of a part of i. (k) Image reconstructed with online learning. (l) Zoomed in version of a part of k.	50
3.16	Result of the third experiment with $L \approx 0.66$. (a) Reconstructed image with full data. (b) Zoomed in version of a part of a. (c) Conventional reconstruction. (d) Zoomed in version of a part of c. (e) Image reconstructed with point-region enhanced regularization. (f) Zoomed in version of a part of e. (g) Image reconstructed with overcomplete DCT. (h) Zoomed in version of a part of g. (i) Image reconstructed with offline learning. (j) Zoomed in version of a part of i. (k) Image reconstructed with online learning. (l) Zoomed in version of a part of k.	51
4.1	Synthetically constructed test Image. (a) Low-rank background part. (b) Sparse part. (c) Composite image.	60
4.2	Result of the first experiment with $L = 0.88, 0.76, 0.66$ for the first, second and third columns respectively. Conventional reconstruction (first row). Point-region enhanced reconstruction (second row). The composite image produced by the proposed approach (third row). The sparse component produced by the proposed approach (fourth row). The low-rank component produced by the proposed approach (fifth row).	62
4.3	Result of the first experiment with $L \approx 0.90$. (a) Reconstructed image with full data. (b) Conventional reconstruction. (c) Image reconstructed with point-region enhanced regularization. (d) Proposed method: Composite image. (e) Proposed method: sparse image. (f) Proposed method: low-rank image.	65

4.4	Result of the second experiment with $L \approx 0.77$. (a) Reconstructed image with full data. (b) Conventional reconstruction. (c) Image reconstructed with point-region enhanced regularization. (d) Proposed method: Composite image. (e) Proposed method: sparse image. (f) Proposed method: low-rank image.	66
4.5	Zoomed in version of the second experiment. (a) Reconstructed image with full data. (b) Conventional reconstruction. (c) Image reconstructed with point-region enhanced regularization. (d) Proposed method: Composite image. (e) Proposed method: sparse image. (f) Proposed method: low-rank image.	67
4.6	Result of the third experiment with $L \approx 0.71$. (a) Reconstructed image with full data. (b) Conventional reconstruction. (c) Image reconstructed with point-region enhanced regularization. (d) Proposed method: Composite image. (e) Proposed method: sparse image. (f) Proposed method: low-rank image.	68

List of Tables

3.1	Parameters and their values used in synthetic and real SAR scene experiments.	36
3.2	Reconstruction performance of the methods on real SAR scenes in terms of MSE.	52
4.1	Reconstruction performance of the methods on synthetic SAR scenes in terms of MSE.	61

Chapter 1

Introduction

This thesis presents two new approaches for synthetic aperture radar (SAR) image reconstruction. In this chapter, we first introduce the SAR imaging problem and discuss the motivation of this thesis. We then provide a concise description of the technical contributions of this thesis. Finally, we present an outline of the thesis.

1.1 Problem Definition and Motivation

Synthetic aperture radar (SAR) is a sensor type that offers several advantages for remote sensing applications. Firstly, it illuminates the field which enables the use of SAR day and night. Secondly, it uses microwaves which are robust to weather conditions such as cloud and rain. Finally, SAR can provide high resolution images by collecting data from different viewing angles. Therefore, there is a growing importance to SAR systems for many applications because of its availability for all weather conditions and high resolution results. SAR systems use an airborne or spaceborne sensor for imaging the target field. In an airborne SAR system, while the aircraft moves along its flight path, the sensor transmits microwave pulses. Some of these pulses are reflected from the ground back to the sensor. The SAR sensor receives these signals. This process is repeated for many aperture positions as the aircraft moves. These collected signals from different view angles are synthesized for imaging the reflectivity field. SAR data collection is illustrated in Figure 1.1. SAR data involves pre-processing steps such as demodulation and windowing. The SAR imaging problem is the problem of reconstructing

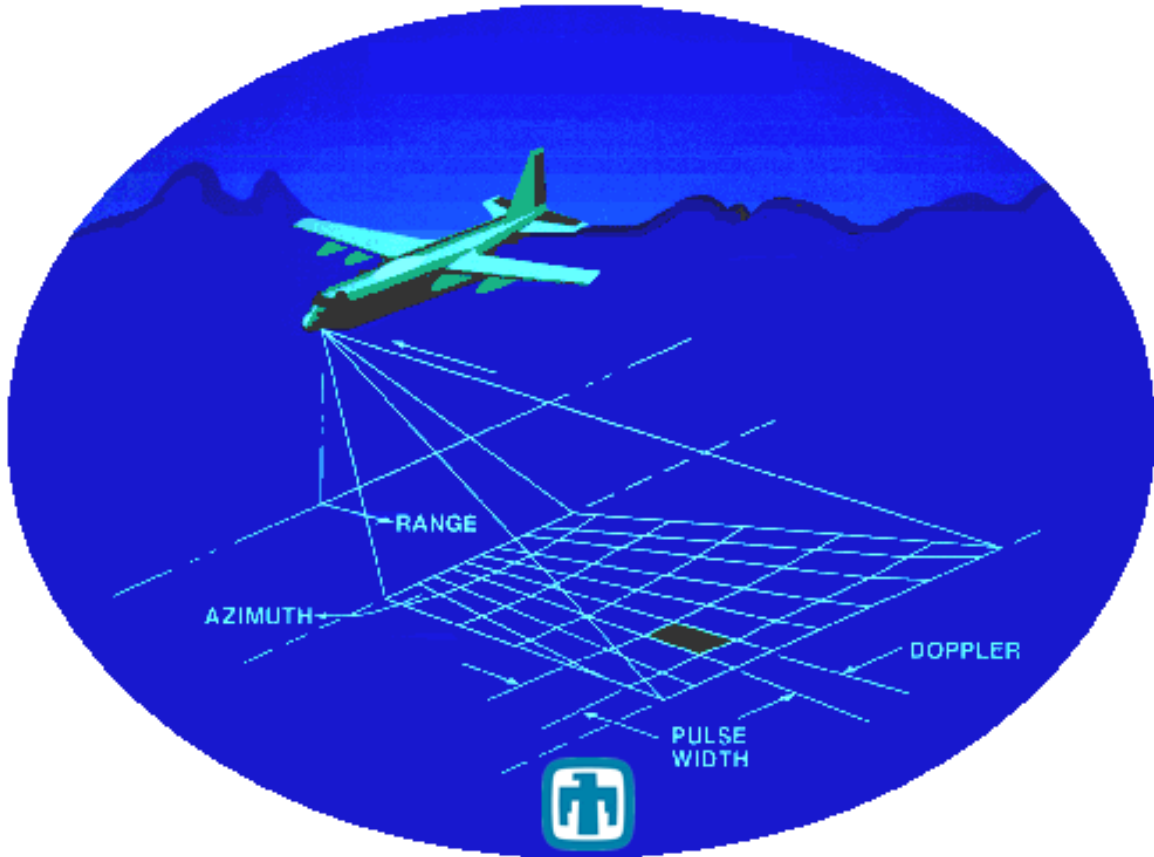


Figure 1.1: SAR data collection geometry. (Image obtained from the web site of Sandia National Laboratories.)

tion of the reflectivity field (image to be reconstructed) from the pre-processed SAR data.

The history of SAR goes back to more than half a century [51]. Nevertheless, both hardware and signal processing methods for SAR systems involve active areas of research, mostly driven by new applications and mission requirements. One of the well known spaceborne SAR systems called TerraSAR-X [4] provides high resolution earth images with wide angles. This system features a recently launched mode called staring spotlight mode for SAR imaging. This mode can provide a high resolution image of a wide area with up to 25 cm resolution. These images can provide complementary information to the optical images since reconstructed SAR images from return of microwave signals can involve special characteristics of the field. An example SAR image obtained

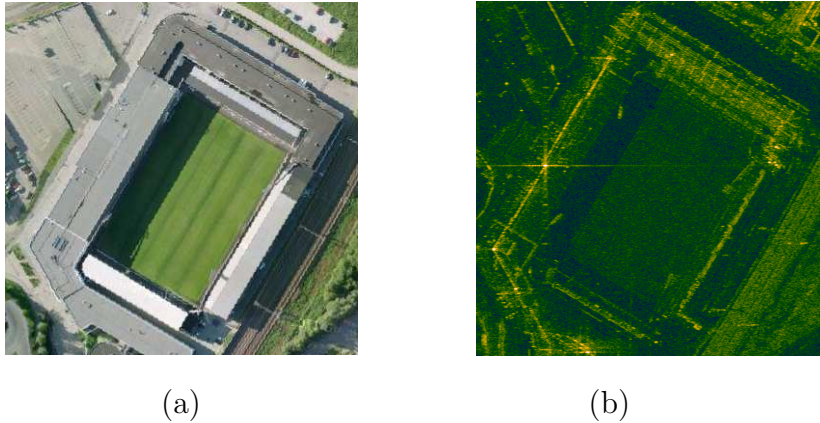


Figure 1.2: Arasen stadium, Norway. (a) Google Earth. (b) Conventionally reconstructed SAR image.

from this mode is shown in Figure 1.2 along with the Google Earth photograph of the field.

Once a SAR image is formed, it can be used for decision or interpretation. SAR images have been used for a variety of applications in both military and civilian settings. SAR images are used for target recognition, and environmental monitoring such as sea-ice, cultivation, and oil spill to the ocean. These applications usually require high resolution images for accurate decision or interpretation. Thus, image formation of SAR data comes into prominence. Current SAR systems achieve image formation by using Fourier transformation-based algorithms [12, 39]. These data-driven conventional image formation algorithms are simple and efficient. However, they suffer from noise, speckle limited-resolution, and sidelobe artifacts due to the limited bandwidth of the SAR systems. Conventional methods do not involve any prior information related to the field. Artifacts appearing of conventional reconstructions may complicate the performance of the SAR imaging tasks. For example, noisy SAR image may deteriorate a segmentation process for object recognition.

Therefore for better interpretation of the SAR images for a particular task, well reconstructed SAR images are required. Once SAR image problem considered as typical ill-posed linear inverse problem, several regularization methods have been proposed [19, 64, 14] and proven to offer better reconstruction quality as compared to conventional

methods by integrating prior information to the SAR image reconstruction framework. These methods provide accurate results by combining reduced data of the reflectivity and prior information such as sparsity on the characteristics of the image.

To summarize, quality of the image reconstruction depends to two elements of the problem: Data and statistical prior information about the scene to be imaged. The first one can improve the reconstruction process as better SAR system modes and hardware architectures are presented while the latter one can improve the reconstruction of image by proposing better representations for the prior term. Throughout the thesis, we will focus on the latter one.

1.2 Contributions of this Thesis

As we mentioned before, adding prior information into the SAR image reconstruction framework improve the overall reconstruction as long as the prior information fits with the actual image. Most of the regularization methods use a prior term such that the image is assumed to be sparsely represented in terms of a predefined dictionary. If in fact, this assumption holds, i.e. the dictionary contains features of the original image, then the reconstructed image will be more accurate than the conventionally reconstructed one. However, if the original image does not lend itself to accurate sparse representation by the predefined dictionary, the reconstruction task becomes more challenging. Thus learning the dictionary for better representation of the images turns out to be an important issue which will be one of the two main focuses of this thesis.

The first contribution of this thesis is the development of dictionary learning-based SAR image reconstruction framework. Rather than predefined prior terms such as Wavelet dictionary, 2D gradient approximation operator, our framework learns the features of image in online manner. We also proposed an offline framework where the dictionary is learned from training patches of SAR images.

The second contribution of this thesis is a framework and an associated algorithm that separates the background which is assumed to be low-rank from sparse features of the field while reconstructing the original image. Our approach has the potential to

provide an improvement for many interpretation tasks of SAR images since separating low-rank texture and sparse regions are done during the reconstruction process.

1.3 Organization of the Thesis

In Chapter 2 we provide background material on SAR imaging, sparse representation, dictionary learning, and low rank matrix recovery. Chapter 3 contains the first contribution of this thesis, namely a dictionary learning-based approach for sparsity-driven SAR imaging. Chapter 4 contains the second contribution of this thesis, namely a formulation and an associated algorithm for SAR imaging based on low-rank sparse decomposition. In chapter 5 we summarize and discuss the results of this thesis and suggest several potential future directions.

Chapter 2

Background

In this chapter, we provide preliminary information on SAR imaging and sparse signal representation. We describe the basic principles of SAR and present the mathematical observation model for spotlight-mode SAR. We provide some background on sparse signal representation and compressed sensing (CS). We then describe existing SAR image formation methods including those exploiting sparsity. We introduce dictionary learning for sparse representation. Finally, we review recent ideas on the decomposition of matrices into their sparse and low-rank components.

2.1 Synthetic Aperture Radar Basics

2.1.1 Principles of SAR Imaging

Conventional radars were developed mainly for object-detection. They were mainly used for military purposes such as detecting and tracking aircraft, vehicles, and tanks. However, in modern world, radars are used for many civilian applications including traffic control, imaging a terrain, and meteorological monitoring. Two objects that reside in different ranges from the radar can be distinguished by the radar. The main principle of radars is simple and unknowingly has been used for people when they try to figure out the depth of a well. They drop a stone and wait for its echo knowing that the duration of the waiting time is proportional to the depth of the well. Correspondingly, radar antenna or sensor transmits high-bandwidth pulses and collects returned signals. Knowing the speed of the signal implies knowing the range of the target. These high-

bandwidth pulses used by radar antenna provide high range resolutions and they are robust to all weather conditions such as cloud and rain which makes radar systems preferable. However, for imaging of say a 2D spatial field, two objects at the same distance from the radar but residing in different directions should be distinguished as well. Capability of distinguishing such two objects is determined by the cross-range (azimuth) resolution of the radar. Cross-range resolution of a radar can be expressed as follows:

$$\rho_y = \frac{R\lambda}{d} \quad (2.1)$$

where R is the distance between the radar and the target (range), λ is the wavelength of the source, and d is the size of the antenna aperture. With a simple calculation, it can be observed that, for X-band radar operating at a 30 km range with a typical wavelength of 3 cm, 1 m resolution capability requires a 900 m physical antenna. In other words, distinguishing vehicles or tracks on ground patch requires an unfeasibly large antenna.

Synthetic aperture radar (SAR) achieves this required resolution capability by sending multiple pulses and collecting the received signals from different observation points. In particular, it synthesizes the effect of a large antenna by using multiple observations of a small antenna [13]. Small antenna travels the required path by means of an aircraft. SAR systems provide high cross-range resolutions and they can operate both day and night. Thus, SAR imaging with its capability of high cross-range resolution has become an important technology in remote sensing.

Stripmap-mode SAR and spotlight-mode SAR are two distinct modes in which a SAR system can operate. In stripmap-mode SAR radar, the platform uses a fixed antenna. Therefore, radar scans the ground as the aircraft flies. On the other hand, in spotlight-mode SAR, the physical antenna is steered to the ground patch to be imaged so as to illuminate the same terrain continuously [39]. Spotlight-mode SAR provides higher resolution since the same terrain is observed from many angles. Recently, staring spotlight-mode SAR has been used on the TerraSAR-X radar, which is capable of providing a resolution of up to 25 cm. Hence these high resolution SAR images provide complementary information to the optical images. We show the geometry for data

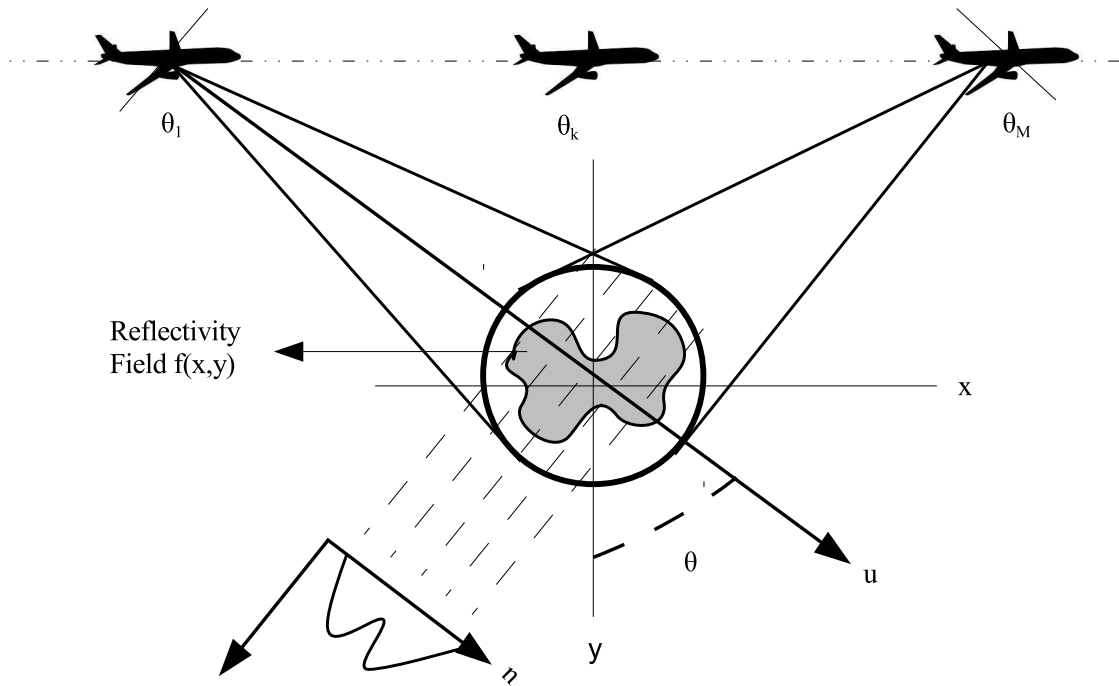


Figure 2.1: Ground-plane geometry for spotlight-mode SAR.

collection in spotlight-mode SAR in Figure 2.1. The x coordinate represents azimuth (cross range) and the y coordinate which is parallel to the flight path represents range. The reflectivity field f is illuminated by a radar RF beam. As the airborne radar travels its path by means of an aircraft, for particular azimuth angles θ_k , high-bandwidth pulses are transmitted and echoes are received. Then these signals are processed. As illustrated in Figure 2.1, SAR returns at a particular observation point provide a projectional view of the scene after some pre-processing steps which we describe in the following section.

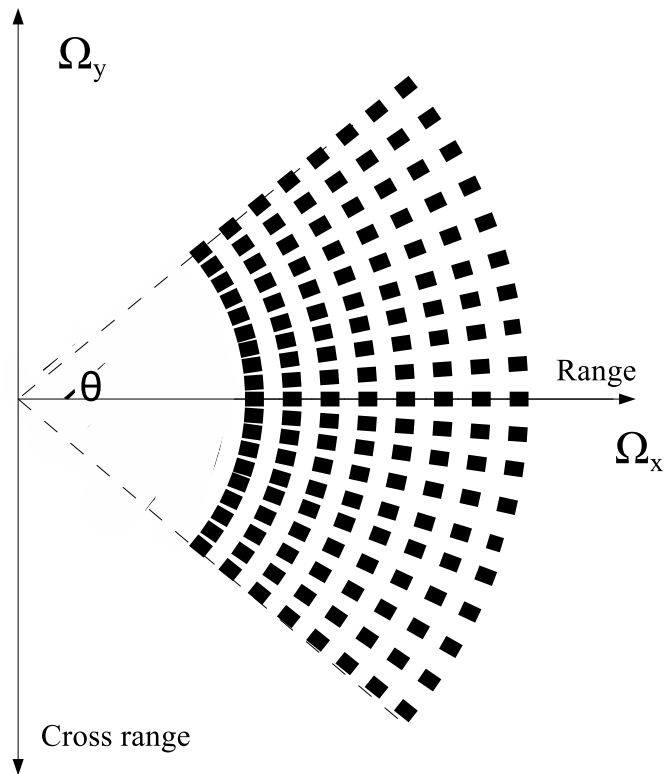


Figure 2.2: Graphical representation of the support of the known phase history data samples in 2D spatial frequency domain.

2.1.2 Spotlight-mode SAR Signal Model

In this section we briefly describe the tomographic formulation of spotlight-mode SAR following the development in [39]. Let $f(x, y)$ be the complex-valued reflectivity field (image to be reconstructed). SAR sends and collects returned signals to this field as it traverses its flight path. A common signal transmitted in SAR is the FM chirp pulse

$$s(t) = \begin{cases} e^{j(w_0 t + \alpha t^2)} & |t| \leq \frac{T_p}{2} \\ 0 & \text{else} \end{cases} \quad (2.2)$$

where w_0 is the carrier frequency, T_p is the pulse duration, and 2α is the FM rate. Return signals for every aperture position are collected by a radar sensor which is continuously

steered to the ground patch. After some pre-processing steps, the relationship between the return signals for a given angle θ and the complex-valued reflectivity field $f(x, y)$ becomes:

$$r_\theta(t) = \iint_{x^2+y^2 \leq L^2} f(x, y) e^{-jK(t)(x \cos \theta + y \sin \theta)} dx dy \quad (2.3)$$

In this equation; L is the radius of the reflectivity field, and $K(t)$ is the radial spatial frequency:

$$K(t) = \frac{2}{c} (w_0 + 2\alpha(t - 2\frac{R_\theta}{c})) \quad (2.4)$$

where c is the speed of the light and R_θ is the distance between radar and reflectivity field at angle θ . Note that, this spatial frequency is limited to a finite frequency interval since the pulse duration and the FM rate is limited. Therefore we can see that $r_\theta(t)$ corresponds to a limited slice from the 2D Fourier transform of the reflectivity field $f(x, y)$ at angle θ . For M observation points, we can formulate the discrete observation model as follows:

$$\underbrace{\begin{bmatrix} r_1 \\ r_2 \\ \vdots \\ r_M \end{bmatrix}}_r = \underbrace{\begin{bmatrix} C_1 \\ C_2 \\ \vdots \\ C_M \end{bmatrix}}_C f \quad (2.5)$$

where r contains phase histories and C contains the discretized approximation to the observation kernel for all of the M observations. These sampled returned signals called phase histories lie on an annular region in the 2D spatial frequency domain which is illustrated in Figure 2.2.

2.2 Image Reconstruction and Sparse Representation

In this section, we explain the need for regularization in solving inverse problems in imaging. We then briefly review compressed sensing theory and sparse representations.

2.2.1 Regularization in Image Processing

For most of the engineering problem such as image restoration, and reconstruction the following discrete observation model

$$g = Hf + n \quad (2.6)$$

has been used in a way that $g \in \mathbb{C}^M$ is measurement vector, $f \in \mathbb{C}^N$ is original image vector, and $H \in \mathbb{C}^{M \times N}$ is a measurement matrix. Generally measurement noise n is also included in the equation. This is a typical inverse problem in imaging where we try to estimate f given the observation vector g . Note that this discrete observation model is also applied in to the SAR imaging problem. Solution of this problem can be found with the least squares approach:

$$\hat{f}_{LS} = \arg \min_f \|g - Hf\|_2^2 \quad (2.7)$$

where $\|\cdot\|_2$ is the l_2 norm. Least squares approach deals with the non-existence of the solution. If the null space of the measurement matrix H is not empty as is the case for the underdetermined problems, the least squares solution is not unique. Choosing the solution that has minimum l_2 norm provides unique solution which is called the least-squares min-norm solution. However, in the presence of noise this solution may not provide the desired solution when H is ill-conditioned. To find a better solution, *a priori* information can be included into the main problem. This type of method is called regularization. A general framework for regularization can be established as follows:

$$\hat{f} = \arg \min_f \phi_{data}(f|g) + \lambda \phi_{prior}(f) \quad (2.8)$$

where $\phi_{data}(\cdot)$ represents the data fidelity term, $\phi_{prior}(\cdot)$ is a prior function that enhances predetermined features of the original image f , and λ is a regularization parameter that balances data and prior terms.

A simple way to use this framework is including a quadratic term as a prior function. This type of method is called quadratic regularization. A general Tikhonov type regularization is [41, 56]

$$\hat{f}_{Tik} = \arg \min_f \|g - Hf\|_2^2 + \lambda \|Lf\|_2^2 \quad (2.9)$$

where L is regularization matrix. Note that, selecting this matrix as identity matrix leads to the Lagrangian form of the generalized solution. Selecting L as an approximation to the 2D gradient operator enforces smooth regions and suppresses noise that provides useful results for piecewise smooth images.

Although quadratic regularization type solutions are computationally efficient and simple, powerful constraints and consequently powerful results are possible by using non-quadratic regularization. Most of the images admit sparse representation in some transform domain. For example, if the image consists of a few nonzero elements, sparse solution is preferable. It has been shown that non-quadratic l_p norm where $p < 2$ provides sparse solutions. One example of this type is using smooth expression of l_p norm [59]:

$$\|f\|_p^p = \sum_i^N (|f_i|^2 + \epsilon)^{p/2} \quad (2.10)$$

where ϵ is small constant for avoiding non-differentiability around 0. Smaller p implies sparser results. Another non-quadratic regularization model commonly used in image processing is total variation (TV) model [48, 52]

$$\hat{f}_{TV} = \arg \min_f \|g - Hf\|_2^2 + \lambda \|\nabla f\|_1 \quad (2.11)$$

where ∇ is gradient operator. TV regularization provides successful results for piecewise constant images and preserves strong edges [59]. Note that TV regularization is a special form of (2.9) where $L = \nabla$ and the norm of the prior term is l_1 norm.

So far we analyzed both non-quadratic and quadratic regularization methods, and in many contexts it can be observed that non-quadratic regularization methods provide better solutions as compared to quadratic regularization methods. One of the constraints we mentioned for the non-quadratic regularization methods is sparsity. Sparsity can be enforced to the image if the underlying scene consists of only a few nonzero elements. Moreover most of the images admit sparsity on some transform domain and using such transform matrices these images can be represented sparsely. Hence powerful results can be obtained by exploiting the sparse feature of the image on some transform domain.

2.2.2 Sparse Representation

As an alternative, an image can be represented with a few coefficients of the sparsifying transform in synthesis-based formulation where image is formed by selecting a few columns of the matrix. This matrix is generally called dictionary. In particular, let $D = [d_1, d_2, \dots, d_N] \in \mathbb{C}^{N \times K}$ be the dictionary where its column d_i is called atom. If $K > N$ this dictionary is called overcomplete. One can represent the signal f with this dictionary as follows:

$$f = D\alpha \quad (2.12)$$

where $\alpha \in \mathbb{C}^K$ is the vector of sparse coefficients in which f is represented with linear combination of the atoms of D . This representation has infinitely many solutions. Therefore, the one with linear combination of few atoms -sparsest- is attractive. General aim becomes trying to represent f with an overcomplete dictionary D sparsely. This sparse representation problem can be expressed in two ways:

$$\min_{\alpha} \|\alpha\|_0 \quad s.t. \quad \|f - D\alpha\|_2^2 \leq \epsilon \quad (2.13a)$$

$$\min_{\alpha} \|f - D\alpha\|_2^2 \quad s.t. \quad \|\alpha\|_0 \leq T \quad (2.13b)$$

where $\|\cdot\|_0$ is the l_0 norm, counting the nonzero elements, ϵ is the sparsity precision and T is the sparsity level. The main difference between two problems is the second one enforces certain level of sparsity while the first one does not. Unconstrained form of the sparse representation problem can be expressed as follows:

$$\min_{\alpha} \lambda \|\alpha\|_0 + \|f - D\alpha\|_2^2 \quad (2.14)$$

where for a particular choice of λ these two equations become equivalent. Solution of the problem (2.14) is generally called sparse coding. Note that because of the l_0 norm, this problem is non-convex and solution is NP-hard so that pursuit algorithm can be used in order to solve this problem.

Several greedy algorithms are proposed for sparse coding. Matching pursuit [38] and orthogonal matching pursuit (OMP) [40] are well known greedy algorithms for sparse coding. OMP selects a dictionary atom having the largest support on the data and estimates its corresponding coefficient using a least squares approach. The OMP algorithm

for a certain sparsity threshold is explained in Algorithm 1. Note that the error bound between the original signal f and the sparsely represented one $D\alpha$ can also be used as a stopping criterion. These pursuit algorithms are simple and computationally efficient. As an alternative one can solve the following sparse coding problem by relaxing the sparsity term in order to make the problem convex:

$$\min_{\alpha} \lambda \|\alpha\|_1 + \|f - D\alpha\|_2^2 \quad (2.15)$$

This problem is the Lagrangian form of a well known problem in statistics, the least absolute shrinkage and selection operator (LASSO) [55]. This convex sparse coding problem can be solved via basis pursuit (BP) [17]. The focal under-determined system solver (FOCUSS) [27] solves the sparse coding problem (2.14) by replacing the l_0 norm with an l_p norm where $p < 1$. Thus, FOCUSS provides powerful results but small p leads to a non-convex problem and computational inefficiency.

Algorithm 1 Orthogonal matching pursuit (OMP) algorithm

Input: $f \in \mathbb{C}^N, D = [d_1, d_2, \dots, d_K] \in \mathbb{C}^{N \times K}, T$

Initialization: $r = f, i = 0, \alpha = 0 \in \mathbb{C}^K, S = \emptyset$

while $i \leq T$ **do**

$k = \arg \max_i d_i^T r$

$S = S \cup k$

$\alpha = \arg \min_{\alpha} \|f - D\alpha\|_2^2 \quad s.t. \quad \alpha_{S^c} = 0$

$r = f - D\alpha$

$i = i + 1$

end while

Output: Sparse Coefficients α

2.2.3 Compressed Sensing

In the previous section we introduced sparsity and sparse recovery algorithms. In this section, we will introduce widely used phenomena in image processing: Compressed sensing (CS) theory [21, 10]. Consider the inverse problem of (2.6) where $M < N$.

Assuming that unknown signal f can be represented sparsely in some transform domain D i.e. sparsifying dictionary $D = [d_1, d_2, \dots, d_K] \in \mathbb{C}^{n \times K}$ represents f with linear combination of its atoms d_i . CS theory suggests that accurate recovery of the following convex relaxation of the sparse recovery problem

$$\min_{\alpha} \|\alpha\|_1 + \lambda \|g - HD\alpha\|_2^2 \quad (2.16)$$

can be obtained with limited measurements provided that $f = D\alpha$ is T -sparse such that $\|\alpha\|_0 \leq T$ and $\Phi = HD$ satisfies restricted isometry constant (RIC) with constant σ_K such that:

$$(1 - \sigma_K) \|x\|_2^2 \leq \|\Phi x\|_2^2 \leq (1 + \sigma_K) \|x\|_2^2 \quad (2.17)$$

where x is any vector with at most K nonzero entries. Under these conditions CS theory guarantees accurate recovery under limited samples even below Nyquist rate. CS theory senses (recovers) unknown signal f from its underdetermined measurement g while compressing it with a dictionary D . Thus, once a dictionary that compresses the signal to be reconstructed is found, limited linear observations becomes sufficient for reconstruction purposes that makes selection of the dictionary more of an issue. A variety of predetermined overcomplete dictionaries have been proposed and used for sparse representations such as discrete cosine transform (DCT), wavelets, curvelets. These dictionaries are found to be very effective for sparse representations.

2.3 Dictionary Learning

In the previous section, we mentioned that predetermined dictionaries have been used for sparse representations. However, the predetermined characteristic of dictionaries limits effective use of CS on signals that cannot be represented parsimoniously by these dictionaries. Thus, the following question emerges: Can we form an application-based dictionary? This question evoked an area of research under the name of dictionary learning where dictionary atoms are adaptively learned from training sets.

The general problem of dictionary learning can be expressed as follows. Let $\{f_i\}_{i=1}^N$ be the set of signals. We seek an overcomplete dictionary D in order to represent this

set of signals with sparse coefficients $\{\alpha_i\}_{i=1}^N$. Note that, for extremely sparse problems where each signal is represented with only one dictionary atom $\{d_i\}_{i=1}^K$ finding sparse coefficients and dictionary atoms turn out to be the K-means clustering problem [26]. The iterative K-means algorithm assigns each cluster to an atom of D in the first stage by assuming D is fixed and updates elements of D for better clustering. This approach has become the essence of most of the dictionary learning methods recently. In particular, dictionary learning methods involve two stages: Sparse coding and dictionary update.

There are several dictionary learning methods such as probabilistic approaches [32, 33], and method of optimal directions (MOD) [23] (see [2, 47] for details). Recently, a dictionary learning method called K-SVD [3] has been used widely in imaging applications. We introduce K-SVD in the next section.

2.3.1 K-SVD

We now explain the details of the K-SVD algorithm. Let $F = \{f_i\}_{i=1}^N$ be the set of training signals and $\Gamma = \{\alpha_i\}_{i=1}^N$ be the sparse coefficients matrix. Then, the sparse representation problem in (2.13) takes the form of

$$\min_{\alpha, D} \|F - D\Gamma\|_F^2 \quad s.t. \quad \forall i \quad \|\alpha_i\|_0 \leq T \quad (2.18)$$

¹ Note that this problem involves N sparse representation problems hence dictionary D is subject to update adaptively. K-SVD iteratively updates sparse coefficients and dictionary via two steps: the sparse coding stage and the codebook update stage. Former stage requires the solution of N sparse recovery problems. While keeping dictionary D fixed, sparse coefficients are updated by using OMP. Note that, any pursuit algorithm that we mentioned in Section 2.2.2 can be used in that stage. In the codebook update stage, dictionary atoms $\{d_i\}_{i=1}^K$ and the corresponding sparse coefficients are updated sequentially. In particular, assuming that Γ and D are fixed except the i^{th} dictionary atom and its corresponding sparse coefficients α_i^T (i^{th} row of Γ), then the penalty term

¹Please note that unlike its use in Section 2.2, the variables f_i, N in this section denote training signals and number of training signals respectively. The distinction should be clear from context

for that dictionary atom takes the form of

$$\left\| \left(F - \sum_{j \neq i}^K d_j \alpha_j^T \right) - d_i \alpha_i^T \right\|_F^2 = \|E_i - d_i \alpha_i^T\|_F^2 \quad (2.19)$$

where E_i represents the error induced by the of $K-1$ terms when the i^{th} term is removed from the dictionary. K-SVD sequentially updates all dictionary atoms d_i and α_i^T so as to minimize this penalty term. Note that, $d_i \alpha_i^T$ is a rank-1 matrix. Indeed, this property makes K-SVD distinctive from other dictionary learning methods. Singular value decomposition (SVD) is used for finding an alternative d_i and α_i^T . SVD finds a rank-1 matrix that effectively approximates the error matrix E_i . However, this approach may damage the sparsity of α_i . Therefore, by defining following set

$$w_i = \{j | \alpha_j \neq 0, \quad 1 \leq j \leq K\} \quad (2.20)$$

the update step is restricted to the nonzero indices of the sparse coefficients. Defining a selection matrix Ω_i such that its $(w_i(j), j)$ entries are one and other entries are zero. Using this matrix, the penalty term becomes

$$\|E_i \Omega_i - d_i \alpha_i^T \Omega_i\|_F^2 = \|\widetilde{E}_i - d_i \widetilde{\alpha}_i^T\|_F^2 \quad (2.21)$$

where \widetilde{E}_i represents error columns in which the dictionary atom d_i is used. Hence zero entries are discarded from the rank-1 matrix. In that way the sparsity condition of the sparse coding stage is preserved. Then, \widetilde{E}_i is decomposed to $U \Sigma V^T$ by using SVD. The first column of U is assigned to d_i and the first column of V multiplied with the first singular value $\Sigma(1, 1)$ is assigned to sparse coefficient $\widetilde{\alpha}_i$. This SVD is applied for all K dictionary atoms sequentially. Therefore, this method is called K-SVD. Note that the main difference between K-SVD and other dictionary learning methods is it updates both the dictionary and the sparse coefficients in the codebook update step. Steps of K-SVD are listed in Algorithm 2.

K-SVD has been widely used for many imaging applications [22, 45, 20] and it is reported that it provides strong results on learning application specific dictionaries. However, it has not yet had a significant presence in SAR imaging. We present a preliminary usage of K-SVD in SAR imaging in Section 2.4.3. We will discuss the usage of K-SVD in the SAR image reconstruction concept in Chapter 3.

Algorithm 2 The K-SVD algorithm

Input: Initial dictionary: $D^{(0)}$, Data: $F = \{f_i\}_{i=1}^N$, Sparsity level: T .

Output: Sparse coefficients: $\Gamma = \{\alpha_i\}_{i=1}^N$, Learned dictionary D .

Problem: $\min_{\alpha, D} \|F - D\Gamma\|_F^2 \quad s.t. \quad \forall i \quad \|\alpha_i\|_0 \leq T$

while Stopping criteria is not satisfied **do**

1. **Sparse Coding Stage**

Solve the following problem by OMP algorithm for $i = 1, 2, \dots, N$.

$$\min_{\alpha} \|f_i - D\alpha_i\|_2^2 \quad s.t. \quad \|\alpha_i\|_0 \leq T$$

2. **Codebook Update Stage**

Update each dictionary atom d_i and its corresponding sparse coefficients sequentially using the following procedure.

Calculate error matrix E_i by using the following relation

$$E_i = F - \sum_{j \neq i}^K d_j \alpha_j^T$$

Define set of indices w_i that indicate training samples which use the dictionary atom d_i

$$w_i = \{j | \alpha_j \neq 0, \quad 1 \leq j \leq K\}$$

Calculate \widetilde{E}_i by extracting only the columns corresponds to w_i .

Decompose \widetilde{E}_i to $U\Sigma V^T$ via SVD.

Assign the first column of the U to the dictionary atom d_i and update nonzero entries of corresponding sparse coefficients with the first column of V multiplied with $\Sigma(1, 1)$.

end while

2.4 SAR Image Reconstruction Methods

The SAR imaging problem can be interpreted as linear inverse problem of the form (2.6) where the reflectivity field is reconstructed from noisy and underdetermined measurements of returned signals from the scene. In this section we explain SAR image reconstruction methods for this ill-posed problem.

2.4.1 Conventional Methods

Based on equation (2.3), we observed that phase histories and unknown reflectivity field are related through a band-limited Fourier transform. Thus, early SAR imaging algorithms exploited this relationship. The most widely used SAR image formation algorithm is the polar format algorithm (PFA) [12]. PFA is based on the 2D inverse Fast Fourier transform (FFT). First, phase history samples shown in Figure 2.2 are interpolated from the polar to the Cartesian grid. After interpolation inverse 2D FFT is applied. In order to reduce sidelobes, windowing can be applied before the inverse 2D FFT. Another well-known algorithm is filtered backprojection (FBP) [39]. Similar to PFA, this algorithm does not use prior information. FBP exploits the tomographic formulation of SAR. These algorithms are simple and computationally efficient. Therefore, these algorithms are used in many radar imaging applications. Thus, we called these methods conventional methods.

Although conventional methods are tempting to use because of their simplicity and efficiency, they suffer from noise, speckle, limited resolution, and sidelobes. These algorithms do not include any prior information about reflectivity field.

2.4.2 Sparsity-driven SAR Image Reconstruction Methods

As we expressed repeatedly in Section 2.2 ill-posed inverse problems can be well reconstructed by adding prior information to the objective function. We see that, sparsity-driven reconstruction methods assume that underlying reflectivity admits sparsity in a particular domain. In SAR imaging, sparsity-driven reconstructions have proven to be very effective. Here we discuss both analysis-based formulations where sparsity

is imposed on the features of the reflectivity and synthesis-based formulations where reflectivity is represented sparsely with a dictionary by imposing sparsity on the coefficients of representation through a dictionary.

In [14] an analysis model is proposed for sparsity-driven SAR imaging. The objective function in [14] has the following form:

$$\hat{f} = \arg \min_f \|g - Hf\|_2^2 + \lambda_1 \|f\|_p^p + \lambda_2 \|L|f|\|_p^p \quad (2.22)$$

where λ_1 and λ_2 are regularization parameters and L is discrete gradient approximation. In this function, the first term enforces data fidelity, the second term enforces sparsity on the point scatterers when $p < 2$, and the third term enforces sparsity on the gradient of the magnitude of the reflectivity. As we mentioned previously on TV and Tikhonov regularization, enforcing sparsity on the gradient leads to be piecewise smooth solutions. However, in this model sparsity is imposed on the magnitude of the reflectivity. This is because the phases of the reflectivities are highly random and spatially uncorrelated. Hence imposing sparsity on the real and imaginary parts (which would be the more straightforward approach) may not lead to the desired effect of smoothing out reflectivity magnitudes in homogeneous regions. This model tries to enhance two features: Point-based structures such as point scatterers and man-made sparse structures, and region-based features such as spatially distributed objects, including, e.g., buildings. Sparsity is enforced with l_p norm, with p chosen around 1 or smaller than 1. In the remainder of our discussion, we will call this approach point-region enhanced non-quadratic regularization. If the underlying scene exhibits these two features, this model provides strong reconstruction results. Hence if underlying scene contains only point scatterers, this algorithm provide accurate results with highly underdetermined cases. This algorithm is solved with quasi-Newton type numerical method with particular Hessian scheme using a smooth approximation of l_p norm (2.10).

An alternative of the approach described above is using a synthesis-based sparse representation framework for SAR imaging. However, complex-valued and potentially random-phase nature of SAR reflectivities make the formulation of a sparse representation-based framework for solving the inverse problem of SAR image forma-

tion just a bit more challenging than inverse problems involving real-valued fields, such as those appearing several medical imaging applications. The recent work in [49] proposes a synthesis-based sparse representation framework for SAR imaging that involves solving the magnitude and the phase of the reflectivities separately. This approach paves the way for using overcomplete dictionaries to represent the magnitude of the reflectivity field sparsely. In particular, introducing the notation $f = \Theta |f|$, where Θ is a diagonal matrix containing the unknown phase of the reflectivity in exponentiated form and $|f|$ represents the magnitude of the reflectivity, represented by an overcomplete dictionary Ψ such that $|f| = \Psi\alpha$, [49] poses the following joint optimization problem for SAR image formation:

$$\hat{\alpha}, \hat{\Theta} = \arg \min_{\alpha, \Theta} \|g - H\Theta\Psi\alpha\|_2^2 + \lambda \|\alpha\|_p^p \quad s.t. \quad \forall i \quad |\Theta_{(i,i)}| = 1 \quad (2.23)$$

where α denotes the sparse coefficients and λ is a regularization parameter balancing data fidelity and reflectivity magnitude sparsity in terms of dictionary Ψ . This problem can be solved using a coordinate descent approach with two update steps. In the first stage, sparse coefficients are updated. The second step involves estimation of the unknown phase. Using a number of dictionaries such as wavelets, and shape-based dictionaries enhances some features of the magnitude.

The analysis-based model provides accurate reconstructions, but it only enhances two features of the reflectivity field hence it may suppresses non-smooth regions and patterns involved in the scene. Similarly, while synthesis-based approach produces very good results in certain contexts using dictionaries simultaneously representing multiple types of features, one of its limitations is that these dictionaries are predefined and cannot be easily adapted for a certain context in a data-driven manner. Both models do not consider particular characteristics of certain reflectivity fields. They provide accurate results if the reflectivity field corresponds to their pre-defined sparsity constraints. This problem can be resolved incorporating the dictionary learning ideas discussed in Section 2.3 into the sparsity-driven SAR imaging framework. We propose such an approach in Chapter 3.

2.4.3 Recent SAR Image Reconstruction Methods

Recent sparsity-driven SAR imaging problems can be divided into two groups. The first group is regularization-based frameworks as discussed in Section 2.4.2. There are also preliminary usage of learning-based frameworks in SAR imaging. In [1] incomplete SAR data are reconstructed using K-SVD approach as an image inpainting problem. In [31] a dictionary learning algorithm is used for SAR image despeckling. In [28] dictionary learning algorithm has been proposed for SAR image super-resolution. In [53], K-SVD is used in the process of decomposing a SAR image into a spatially sparse and a spatially non-sparse component. Sparsity-driven imaging has also been extended to various variations or extensions of SAR such as inverse SAR (ISAR) [44] and SAR tomography (TomoSAR) where the SAR principle is extended into the elevation direction [64]. Moreover, there exists some preliminary research [63, 18] on SAR imaging based on low-rank sparse matrix decomposition (LRSD). The second group involves probabilistic approaches. In these frameworks, the SAR imaging problem is considered as maximum a posteriori (MAP) problem with a Bayesian perspective. These approaches [43, 61] utilize prior distributions to model the reflectivity field. In [42, 15] recent sparsity-driven SAR imaging methods are reviewed in detail.

2.5 Low-rank Matrix Recovery

2.5.1 Theoretical Background

Recent years have witnessed rapidly increasing interest in matrix completion or recovery problems and in efficient solutions of these problems. Consider a basic survey matrix $M \in \mathfrak{R}^{n \times m}$ where each column consists of ratings for a particular object such as movie and book, each row represents a particular user. Suppose each user has rated a random subset of the objects. Suppose we want to fill this matrix for an automatic recommendation system. At first glance, it seems there is no solution for this ill-posed problem. However, given the fact that this matrix is low-rank with rank r where $r < (n, m)$ one may turn this matrix completion problem into the following optimization

problem

$$\min_F \text{rank}(F) \quad \text{subject to} \quad \Omega(F) = \Omega(M) \quad (2.24)$$

where Ω is the set indices where M has nonzero elements. Note that, this low-rank matrix F has only $r(2n - r)$ degrees of freedom. This problem is NP-hard and involves minimizing the number of nonzero singular values. Recent work on the subject [11, 46] however have proved that the *nuclear norm*, defined as

$$\|F\|_* = \sum_{i=1}^r \sigma_i(F) \quad (2.25)$$

can, under certain conditions, be used as a surrogate convex form of the rank minimization constraint. After this relaxation, the resulting convex optimization problem is given by

$$\min_F \|F\|_* \quad \text{subject to} \quad \Omega(F) = \Omega(M) \quad (2.26)$$

It has been shown that most low-rank matrices can be recovered perfectly with high probability if the observed number of samples is above a certain limit [11]. Note that, there is an interesting relationship between compressed sensing and low-rank matrix completion. In compressed sensing, l_1 norm is used for convex relaxation of the l_0 norm. In other words, rather than minimizing the number of nonzero elements in the vector, the convex problem tries to minimize the sum of the magnitudes of the elements of the vector. Similarly in the low-rank matrix completion problem, minimization of the number of nonzero singular values is relaxed to the sum of the singular values. As we will explain in detail, this similarity can be observed in the process of solving the problems as well.

This problem can be extended to the recovering problem of a corrupted matrix

$$\min_F \|F\|_* + \lambda \|H(F) - g\|_2^2 \quad (2.27)$$

where H is linear mapping operator and λ is Lagrange multiplier. In this case this problem is generally called low-rank matrix recovery. Note that when H is a selection operator this problem turns to a matrix completion problem. Minimizing nuclear norm can be achieved by using semidefinite programming with interior methods [57]. However, for large matrices these methods are inefficient in terms of computation time.

Recently, simple and efficient methods [8, 36] have been developed in order to solve the nuclear norm minimization problem. We will focus on the *singular value thresholding* method and provide its theoretical legitimacy.

2.5.2 Singular Value Thresholding (SVT)

Consider the following nuclear norm minimization problem

$$\min_F \lambda \|F\|_* + \frac{1}{2} \|F - M\|_F^2 \quad (2.28)$$

where $\|\cdot\|_F$ is the Frobenius norm. It is asserted that singular value shrinkage operator $C_\lambda(M)$ is the solution of the above mentioned problem where for SVD of $M = U\Sigma V^T$

$$C_\lambda(M) = UC_\lambda(\Sigma)V^T \quad \text{s.t.} \quad \tilde{C}_\lambda(\Sigma) = \max(\sigma_i - \lambda, 0) \quad \forall i \quad (2.29)$$

This method essentially applies soft thresholding to the singular values of M . Thus it is called singular value thresholding. Proof of $C_\lambda(M)$ being the unique minimizer of (2.28) is straightforward. Let us first note that the subgradient of the nuclear norm has the form of $Y = UV^T + W$ with the following optimality conditions [11]

$$U^T W = 0 \quad , \quad W V = 0 \quad (2.30a)$$

$$\|W\|_2 \leq 1 \quad (2.30b)$$

then, for $\tilde{F} = C_\lambda(Y)$ to be the unique minimizer following condition should hold.

$$0 \in \lambda \partial \|\tilde{F}\|_* + \tilde{F} - M \quad (2.31)$$

Note we can decompose M such that $M = U_1 \Sigma_1 V_1^T + U_2 \Sigma_2 V_2^T$ where Σ_1 and Σ_2 represent singular values greater than λ and smaller than λ respectively. We have $\tilde{F} = U_1 \Sigma_1 V_1^T - \lambda U_1 V_1^T$. Combining these two relation allows us to express $M - \tilde{F} = \lambda U_1 V_1^T + W$ where $W = U_2 \Sigma_2 V_2^T$. Note that, W obeys optimality conditions and therefore \tilde{F} is the unique minimizer.

2.5.3 Alternating Direction Method of Multipliers (ADMM)

Consider the following unconstrained optimization problem

$$\min_x f(x) + g(x) \quad (2.32)$$

where f and g are convex functions, and $x \in \mathbb{C}^n$. This problem can be turned into a constrained optimization problem by using variable splitting method. In particular, a new variable $z \in \mathbb{C}^n$ can be added to the problem as follows:

$$\min_{x,z} f(x) + g(z) \quad \text{s.t.} \quad x = z \quad (2.33)$$

At first glance, this step may seem pointless, but the main idea behind variable splitting is that constrained form of the problem may be solved easier than its unconstrained form by using algorithms such as Augmented Lagrangian Method (ALM) [29]. Hence, variable splitting can be useful when the objective function has a separable structure. Augmented Lagrangian form of this constrained optimization problem is

$$L(x, z, c) = f(x) + g(z) + \langle c, x - z \rangle + \frac{\beta}{2} \|x - z\|_2^2 \quad (2.34)$$

where $c \in \mathbb{C}^m$ is Lagrange multiplier and β is a positive penalty parameter. ALM solves this problem by iterating between (x, z) and c . In particular, solution for iteration k has the following form:

$$\begin{aligned} (x^{(k+1)}, z^{(k+1)}) &= \arg \min_{x,z} L(x, z, c^{(k)}) \\ c^{(k+1)} &= c^{(k)} + \beta(x^{(k+1)} - z^{(k+1)}) \end{aligned} \quad (2.35)$$

However, solution of the subproblem for $(x^{(k+1)}, z^{(k+1)})$ is generally not straightforward, because in general the corresponding subproblem is non-smooth and it involves a non-separable quadratic term.

Instead of a joint solution of (x, z) , one can solve x and z separately for each iteration. In fact, alternating direction method of multipliers (ADMM) [24] solves the problem by alternating between variables as follows:

$$\begin{aligned} x^{(k+1)} &= \arg \min_x L(x, z^{(k)}, c^{(k)}) \\ z^{(k+1)} &= \arg \min_z L(x^{(k+1)}, z, c^{(k)}) \\ c^{(k+1)} &= c^{(k)} + \beta(x^{(k+1)} - z^{(k+1)}) \end{aligned} \quad (2.36)$$

History of ADMM and ALM goes back to half a century ago. However, these methods have recently found use for many applications. In [5] ADMM has been proposed

for distributed optimization. In particular, if the objective function has a separable structure, ADMM can be used by exploiting variable splitting and ALM. Thus, large problems can be solved by updating relatively small subproblems in parallel. In image processing applications, ADMM has found use when the objective function has a separable structure.

2.5.4 Low-rank Sparse Decomposition (LRSD)

Previously described solution for the nuclear norm minimization paved the way for the problem of decomposing a matrix into the low rank and sparse components. For the imaging problem, this can be considered as decomposing an image into the low-rank background and sparse part. Sparse part may consist of the small objects in the image. In particular low-rank sparse matrix decomposition can be expressed as

$$\min_{L,S} \lambda \|L\|_* + \|S\|_1 \quad \text{s.t.} \quad A = L + S \quad (2.37)$$

where λ balances two constraints. Note that this problem is a convex relaxation of rank and l_0 norm minimization. This formulation is also called robust principle component analysis (RPCA) [9]. One may claim that this optimization problem is high dimensional and non-smooth so the solution is not scalable. However, both nuclear norm and l_1 norm have special structures and they can be separable. Therefore, this problem can be viewed as a separation of low-rank structures from sparse objects of the scene.

Several efficient solutions have been proposed for this problem using gradient descent algorithms such as iterative thresholding [9], the accelerated proximal gradient approach and alternating direction method for augmented Lagrangian method (ALM) [34, 60]. Augmented Lagrangian form of the (2.37) is

$$\min_{L,S} \lambda \|L\|_* + \|S\|_1 + \langle Z, A - L - S \rangle + \frac{\beta}{2} \|A - L - S\|_F^2 \quad (2.38)$$

where Z is the Lagrange multiplier and β is a positive constant. Note that, the objective function has separable structure. Therefore, ADMM can be used for the solution of this problem. Solution is outlined in Algorithm 3. The SLRD framework has recently found use in image processing applications such as face recognition [16], and background

Algorithm 3 Alternating direction methods of multipliers (ADMM) for SLRD

Input: Matrix A that contains both low-rank and sparse features, β , λ .

Output: Sparse matrix S and low-rank matrix L .

while Stopping criteria is not satisfied **do**

1. $S^{(k+1)} = \tilde{C}_{1/\beta}(A - L^{(k)} + \frac{Z^{(k)}}{\beta})$ Soft thresholding
2. $L^{(k+1)} = C_{\lambda/\beta}(A - S^{(k+1)} + \frac{Z^{(k)}}{\beta})$ Singular value thresholding
3. $Z^{(k+1)} = Z^{(k)} + \beta(A - L^{(k+1)} - S^{(k+1)})$ Lagrange multiplier update

end while

subtraction [7]. Some preliminary ideas have been reported for SAR imaging as well [63, 18]. We will integrate this framework into the SAR imaging problem in Chapter 4.

Chapter 3

Dictionary Learning for Sparsity-Driven SAR Imaging

In this chapter, we formulate our SAR image reconstruction framework by integrating patch-based dictionary learning into the sparsity-driven SAR imaging model described in the previous chapter. We introduce using an adaptive dictionary for representing magnitudes of the complex-valued SAR reflectivities. This dictionary can be learned from training data in an offline manner or from test data in an online manner. We present an iterative algorithm for the solution of the optimization problem emerging in our framework for dictionary learning-based SAR image formation. Furthermore, we present experimental results on both synthetic scenes and real scenes from the TerraSAR-X data-set [4].

3.1 Proposed Dictionary Learning Framework

In order to formulate a sparse representation-based framework with a dictionary that sparsely represents the data for solving the inverse problem of SAR image formation, one should consider following facts:

- SAR exhibits complex-valued and potentially random phase reflectivities.
- Large size images require computationally inefficient large dictionaries for the sparse representation.
- In SAR imaging applications, sample scenes representing the ground truth reflectivities are usually not available.

Firstly, the problem of SAR scenes exhibiting random phase can be overcome by representing the magnitude of the complex-valued field by sparsifying dictionaries as in [49, 50], and as described in Chapter 2. Using the notation of $f = \Theta |f|$ the random phase and the magnitude of the complex-valued reflectivity field f can be represented separately where Θ is a diagonal matrix containing the unknown phase of the reflectivity in exponentiated form. In particular $\Theta_{(j,j)} = e^{j\phi_j}$ where ϕ_j is the unknown phase of the j^{th} element of f . The second problem arises when the size of the image to be reconstructed is large. For example, if we reconstruct a 128×128 image, at least a dictionary of size 16384×16384 is required. For an overcomplete dictionary an even larger size is required. Therefore, a patch-based sparse representation [22] can be preferred for computational efficiency. Patch-based dictionaries learned by K-SVD have been used in many imaging applications [62, 37]. In particular, one can represent the small patches of the reflectivity field with a relatively small sized sparsifying dictionary. Small patches extracted with a patch extraction operator E_i are assumed to be represented sparsely with a dictionary D (e.g, $E_i |f| \approx D\alpha_i \quad \forall i$). The third problem is caused by the nature of the SAR system. Observed signals suffer from noise and reconstructed image from these signals contains certain level of noise. Moreover, due to the limited bandwidth of the SAR systems, SAR images suffer from sidelobes, artifacts, and speckle. Therefore, learning a sparsifying dictionary from these data may result in imperfect learning of the features of the reflectivity field. Several pre-processing steps may be required in order to suppress noise and artifacts. These pre-processing steps will be discussed in Section 3. Considering the above mentioned problems, we define the following joint problem for dictionary learning and image formation.

$$\begin{aligned} \left\{ \widehat{|f|}, \widehat{\Theta}, \widehat{D}, \widehat{\alpha}_i \right\} = \arg \min_{|f|, \Theta, D, \alpha_i} & \lambda \|g - H\Theta |f|\|_2^2 + \sum_i \|E_i |f| - D\alpha_i\|_2^2 + \sum_i \mu_i \|\alpha_i\|_0 \\ & \text{s.t.} \quad |\Theta_{(j,j)}| = 1 \quad \forall j \end{aligned} \quad (3.1)$$

In this optimization problem; the first term measures data fidelity, the second term measures the proximity between sparse representations and the magnitude of the image patches, and the third term measures the sparsity of the image patches, where λ is the weight of the data fidelity term. This parameter depends on the measurement

noise and the percentage of the available data. Lastly, Θ is a diagonal matrix where $\Theta_{(j,j)}$ is j^{th} exponentiated phase of the reflectivity field.

Solution of this optimization problem needs a coordinate descent procedure. In order to solve one parameter, other parameters are assumed to be fixed. There are four different parameters to be solved: $|\widehat{f}|, \widehat{\Theta}, \widehat{D}, \widehat{\alpha}_i$. If the dictionary D is learned from several training patches offline, before the image reconstruction process, then the formulation decomposes into sequential steps of offline dictionary learning and online image formation. In this case, the online process would not contain the dictionary as one of its unknowns. For the sake of generality, here we describe the solution of the problem as online learning. Each iteration of this process involves three steps: dictionary learning, phase update, and magnitude update. In the first step, the dictionary D and the sparse coefficients α_i are jointly updated. If the dictionary is learned offline, then in the online process, this step involves just the update of α_i through a pursuit algorithm. The second step minimizes the phase of the reflectivity field by using the iterative method used in [49]. The last step reconstructs the magnitude of the reflectivity field. A Graphical representation of the proposed method is shown in Figure 3.1. Next we explain these three update steps in detail.

3.1.1 Sparse Coefficients and Dictionary Update

This step solves for the patch-based overcomplete dictionary as well as the sparse representation coefficients over that dictionary, while keeping $|f|$ and Θ fixed. More specifically, dropping the constant variables, our subproblem takes the following form:

$$\left\{ \widehat{D}, \widehat{\alpha}_i \right\} = \arg \min_{D, \alpha_i} \sum_i \|E_i |f| - D\alpha_i\|_2^2 + \sum_i \mu_i \|\alpha_i\|_0 \quad (3.2)$$

This subproblem has itself a two steps alternating solution. One solution of this problem is K-SVD [3] as described in Chapter 2. K-SVD solves for the sparse coefficients and the dictionary jointly. In the first step, sparse coefficients are updated through the OMP algorithm and in the second step, each column of the dictionary and sparse coefficients are jointly updated consecutively. In this subproblem, if dictionary D is assumed to be known, e.g, because it has been learned offline, the subproblem has only one type

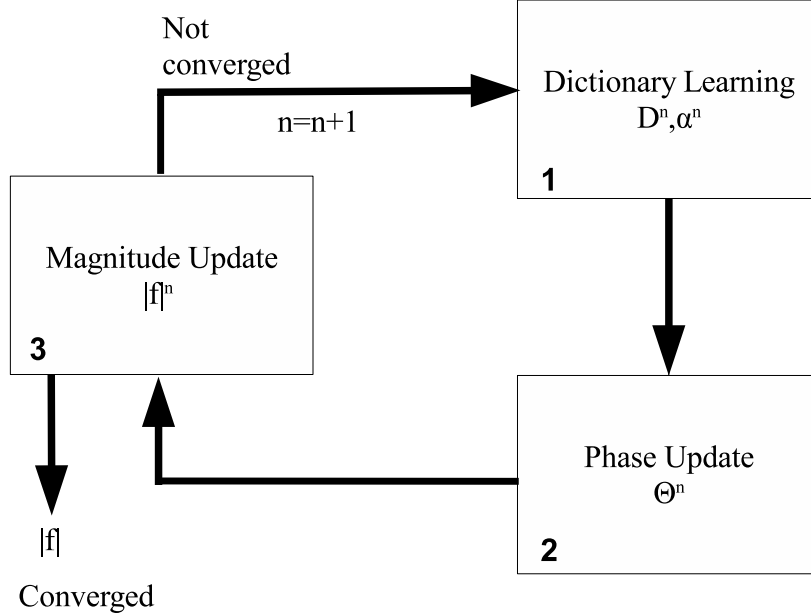


Figure 3.1: Graphical representation of the iterative algorithm.

of unknown which is sparse coefficients. Since minimizing the l_0 norm is not tractable, sparse coefficient can be solved by any given pursuit algorithm as previously mentioned [27, 17, 40]. We will use OMP within our framework since it is computationally efficient and easy to implement.

3.1.2 Phase Update Step

In this step, the phase of the reflectivity field is estimated by keeping the other parameters fixed. This requires solving a subproblem of (3.1) involving the data fidelity term and the constraint only. An algorithm for solving such a phase estimation problem has been proposed in [49, 50], which we utilize in this step. Let us introduce a vector $p \in \mathbb{C}^N$ that contains the diagonal elements of the phase matrix Θ , and the matrix $B \in \mathbb{C}^{N \times N}$ whose diagonal elements contain information about the reflectivity magnitudes.

Let us also invoke the constraint that the magnitudes of the elements of p should be 1, simply because they contain phases in the form $e^{j\phi(f)}$ where $\phi(\cdot)$ denotes the phase. Then, we obtain the following optimization problem in Lagrangian form:

$$\hat{p} = \arg \min_p \|g - HBp\|_2^2 + \lambda_p \sum_{i=1}^N (|p_i| - 1)^2 \quad (3.3)$$

where

$$B = \text{diag} \left\{ \frac{(\sum_i E_i^T D \alpha_i)_k}{(\sum_i E_i^T E_i)_{(k,k)}} \right\} \quad (3.4)$$

and λ_p is a Lagrange multiplier. As mentioned above, B contains information about the current estimate of the reflectivity magnitudes. Here we could use the estimate of $|f|$ from the previous iteration, but instead we choose to incorporate its sparse representation from the current iteration through the α_i . Since this representation is patch-based, (3.4) performs appropriate operations to produce an $N \times N$ matrix, whose N diagonal entries correspond to the N reflectivity magnitudes in the scene. As in [49], we solve this optimization problem through a fixed point algorithm, which can also be shown to be equivalent to a particular quasi-Newton algorithm:

$$G(p^{(n)})p^{(n+1)} = 2(HB)^H g + 2\lambda_p e^{j\phi(p^{(n)})} \quad (3.5)$$

where

$$G(p) = 2(HB)^H(HB) + 2\lambda_p I \quad (3.6)$$

Note that each iteration in (3.5) involves solving a set of linear equations. This is an indication that the approach here solves the non-quadratic optimization problem in (3.3) by turning it into a series of quadratic problems. These linear set of equations can be efficiently solved by the conjugate gradient algorithm with the convergence criterion $\frac{\|p^{n+1} - p^n\|}{\|p^n\|} < \delta_p$

3.1.3 Magnitude Update Step

In this last step, the magnitude of the reflectivity field is estimated keeping the other parameters fixed. The subproblem of (3.1) for updating the reflectivity magnitudes can

be expressed as:

$$|\widehat{f}| = \arg \min_{|f|} \sum_i \|E_i |f| - D\alpha_i\|_2^2 + \lambda \|g - H\Theta |f|\|_2^2 \quad (3.7)$$

This is a quadratic optimization problem with a closed form solution. Taking the derivative with respect to $|f|$ and equating it to zero gives the following equation.

$$\left(\sum_i E_i^T E_i + \lambda \Theta^H H^H H \Theta \right) |\widehat{f}| = \lambda \Theta^H H^H g + \sum_i E_i^T D\alpha_i \quad (3.8)$$

We solve this linear set of equations using the conjugate gradient algorithm. One important point in this step is that the solution of the subproblem may produce complex values. Hence because of the misalignment of the phase, the real part of the solution may be negative. One can propose to convert this problem to into a constrained problem to enforce non-negativity. Non-negativity constraints in sparsity problems have been explored recently and provide an improvement over the final solution [30, 6]. However, this constraint will complicate the solution further. Thus, we simply take the magnitude part of the solution at each iteration.

These three steps are run until the convergence criterion $\frac{\||f|^{n+1} - |f|^n\|}{\||f|^n\|} < \delta_m$ is satisfied. Proof of the convergence of the proposed algorithm is not straightforward. We know that sparse coefficients and dictionary update step minimize the second and third terms of the optimization problem (3.1). Similarly phase update and magnitude update steps minimize the data fidelity term. However, it does not mean that the convergence of the algorithm is guaranteed. We leave the convergence of the proposed method for further research. In experimental results, we have used maximum iteration limit in order to solve convergence problem. The overall algorithm is demonstrated in Algorithm 4.

3.2 Experimental Results

In this section, we demonstrate the effectiveness of our proposed approach for *offline learning* and *online learning* scenarios using both synthetic scenes and real SAR scenes from the TerraSAR-X data-set. We used a band-limited Fourier transform as

Algorithm 4 Structure of the Proposed Algorithm

1. Input: $g, H, \sigma^2, \delta_m, \delta_p, \lambda, \lambda_p$
 2. Initialization: $|f|^{(0)} = |H^H g|, p^0 = e^{j\phi(H^H g)}, n = 0$
 3. Dictionary Learning Stage:
if Offline learning i.e., Dictionary D is known **then**
 Find $\alpha_i^{(n)}$ by using OMP
else
 Find $D^{(n)}$ and $\alpha_i^{(n)}$ by using K-SVD
end if
 4. Phase Update Stage:
Update $\Theta^{(n)}$ by solving (3.5) with CG until $\frac{\|p^{k+1} - p^k\|}{\|p^k\|} < \delta_p$ is satisfied.
 5. Magnitude Update Stage:
Solve (3.8) and update $|f|^{(n)}$
if $\frac{\||f|^{n+1} - |f|^{n}\|}{\||f|^{n}\|} < \delta_m$ **then**
 Return $|f|$
else
 Return to 3.

 $n = n + 1$
end if
-

our forward model H . We provide qualitative results on both synthetic and real SAR scenes, and quantitative results with respect to noise and the percentage of the available data for comparison of our models with three other techniques: Conventional reconstruction [12, 39], point-region enhanced regularization [14], and sparsity-driven SAR image reconstruction with wavelet dictionary. Note that, our algorithm involves some parameters that need to be set. One can tune the parameters for the specific experiment (constant noise and available data). However, when the noise or percentage of the available data changes, these parameters should be considered again. Therefore, for a generic usage of our algorithm, we tried to relate these parameters dynamically with standard deviation of the noise σ and the percentage of the available data L . In particular $L = \frac{N_a}{N_d}$ where N_a is the number of available data samples and N_d is the number of phase history samples in full band-width data.

- **Data fidelity parameter λ :** This parameter balances the data fidelity term and the term which measures the proximity between sparse representations and the magnitude of the image patches in the magnitude update step. These terms are the first and the second terms of the optimization problem respectively. In the presence of high level noise and low available data, the weight of the dictionary should be increased as compared to the observed data. In particular, small value of λ should be selected. On the other hand, if the observed data is reliable such that σ is low and L is high, the weight of the data fidelity term should be increased by selecting a large *lambda*. Therefore, λ is inversely proportional to σ and proportional to L .
- **Phase parameter λ_p :** In the phase update step, this parameter enforces the magnitude of the estimated phase elements to be 1 and as it can be seen from (3.5), λ_p determines the weight of the estimated phase obtained from the previous iteration. We used $p^0 = e^{j\phi(H^H g)}$ for the initial value of the phase where $H^H g$ can be considered as conventional reconstruction. When L is high initial phase is more reliable as compared to the case where L is low. Thus, λ_p is inversely proportional to L . We relate λ_p with $\frac{1}{L}$.

- **Sparsity level and precision** (T, ϵ): Sparsity level T expressed in (2.13) is related to other factors such as power of the dictionary and complexity of the image. Therefore, this parameter should be selected with respect to the dictionary and test image. Sparsity precision ϵ determines how far the current estimate is sparsely represented with respect to the dictionary. When the sparsifying term is more preferable comparing to the data fidelity as in the case of small L and large σ this parameter should be large. Thus it is proportional to L . One can also relate this parameter to σ . However, since the proposed algorithm iterative, in the presence of convergence, it is believed that, noise effect will be reduced iteratively if the algorithm converges to the optimal solution. Therefore, we decrease ϵ slowly at each iteration.

The overall parameters used in both synthetic and real SAR scene experiments are shown in Table 3.1. We present our results in the following two subsections. We present synthetic scene experiments and provide quantitative results of the comparison in Section 3.2.1. We then provide the performance of our approach on real SAR scenes in Section 3.2.2.

Table 3.1: Parameters and their values used in synthetic and real SAR scene experiments.

Parameters	Synthetic scene Experiments	Real SAR scene experiments
λ	$\frac{2L}{\sqrt{\sigma}}$	$\frac{8L}{\sqrt{\sigma}}$
λ_p	$\frac{2}{L}$	$\frac{0.01}{L}$
T	20	35
ϵ	$\frac{0.2}{\sqrt{L}}$	$\frac{0.02}{\sqrt{L}}$
δ_p	10^{-4}	$5 * 10^{-4}$
δ_m	10^{-4}	$5 * 10^{-4}$

3.2.1 Synthetic Scene Experiments

We first demonstrate our approach on 64×64 synthetically constructed scenes. The main advantage of using synthetic scenes is it provides quantitative results for comparison with other techniques and synthetic results generally provide a rough idea about the likely performance of the approach on the real SAR scenes. We add uniformly distributed random phase between $[-\pi, \pi]$ to the data. We take the band-limited discrete Fourier transform of this complex-valued data and finally complex Gaussian noise is added to the data. Final data correspond to the phase history of the SAR data on a rectangular grid. Our aim is to reconstruct an estimate of the original scene by using these simulated phase histories.

For offline learning, an overcomplete dictionary should be generated from the training data. For synthetic experiments we formed 16 64×64 training images. Training patches are extracted from this training set. We use 60000 training patches of 8×8 pixels. Number of atoms of the overcomplete dictionary is chosen to be 441. The reason is we want to compare our approach with the same sized overcomplete Haar dictionary. We show randomly selected 1000 training patches in Figure 3.2. We run the K-SVD algorithm for 200 iterations with the sparsity level $T = 5$. Initial dictionary is selected to be an overcomplete discrete cosine transform (DCT) dictionary. Our offline learned dictionary and the overcomplete Haar dictionary are shown in Figure 3.3 and Figure 3.4 respectively.

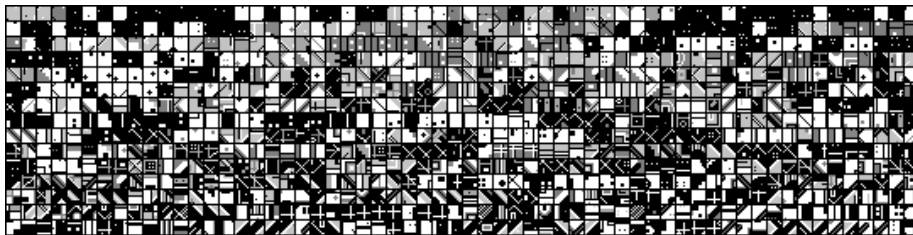


Figure 3.2: Randomly selected 1000 training patches for offline dictionary learning based on synthetic scenes.

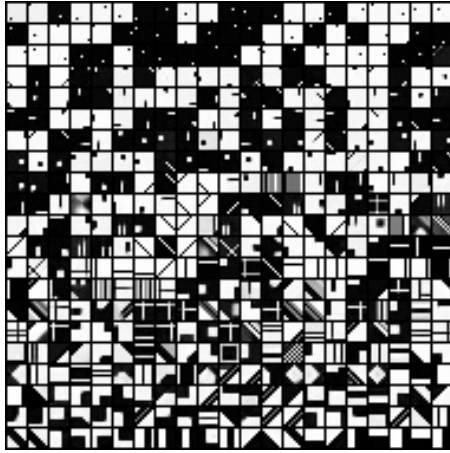


Figure 3.3: Offline learned 64×441 overcomplete dictionary.

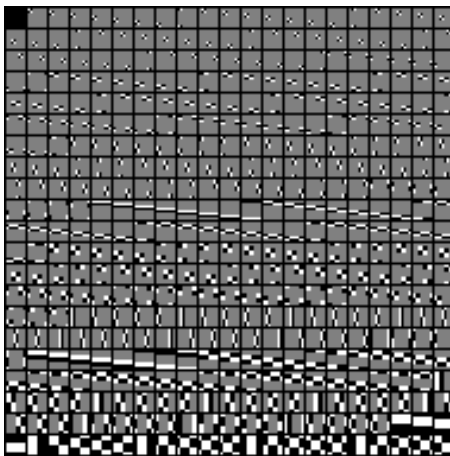


Figure 3.4: Overcomplete 64×441 Haar dictionary.

We first demonstrate the visual performance of our approach and compare it with other 3 methods as mentioned before. For that purpose, a synthetic scene that resembles a SAR scene is constructed. Throughout the all experiments we used $[0, 1]$ scale for images. We deliberately added some patterns in the synthetic images in order to show the effects of our approach. As we explained before, the main rationale of the dictionary learning is dictionaries learned from the training sets may capture some features which are not easily representable in the predetermined transforms such as wavelets, and DCT. All of the algorithms were implemented using non-optimized MATLAB code on an Intel Xeon 2.67GHz CPU. We used $\lambda_1^2 = 10$ and $\lambda_2^2 = 10$ for point region enhanced non-quadratic regularization. For the synthetic experiments we used the parameters shown in Table 3.1. In the first experiment we select $L = 0.9$ such that 90% of the data is available. Reconstruction results are shown in Figure 3.5. In this experiment all of the methods provide reasonable reconstructions except the conventional reconstruction and also we see that overcomplete Haar dictionary-based approach suffers from the diagonal patterns in the image. We then decrease the value of L to 0.8 and 0.7. These results are shown in Figure 3.6 and 3.7 respectively. We can see that both online and offline learning provide better reconstruction compared to the other three methods. Since both point region enhanced non-quadratic regularization and overcomplete wavelet dictionary-based reconstructions are based on the predetermined dictionaries, they fail to reconstruct the genuine diagonal patterns. For the case of $L = 0.7$ we see that offline learning results are better than online learning. The reason is as the image itself deteriorates the performance of the dictionary learned from this image is decreases. We show the online learned dictionaries in Figure 3.8 which validates the previous statement.

We carry out more general experiments in order to see the full picture of the reconstruction performances. We analyze the performance of the methods with varying noise level and L . In particular, we take 5 different synthetic test images unrelated to the training set. These test images are shown in Figure 3.9. Next we perform an experiment such that each image is reconstructed via all of the methods with L decreasing from 1 to 0.5. We then take the average of the reconstruction performances. The performance

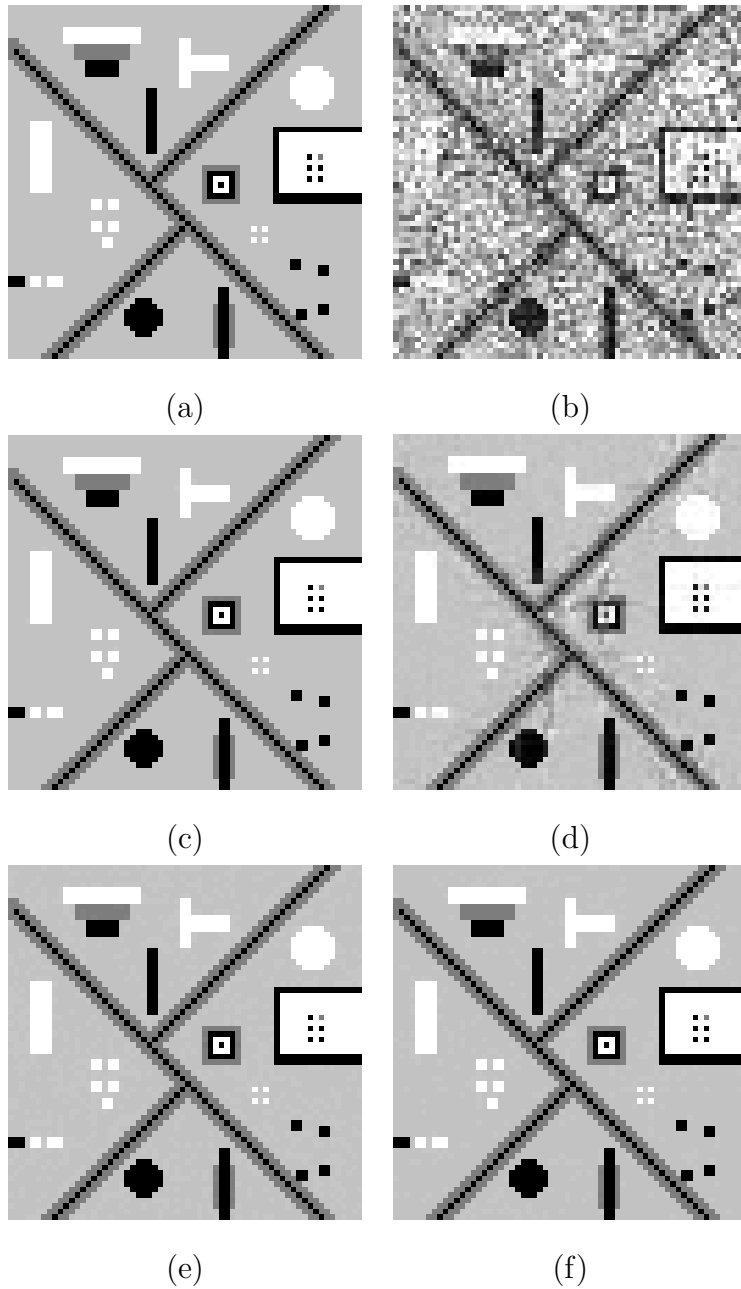


Figure 3.5: Results of the synthetic experiment with available data ratio $L = 0.9$. (a) Original scene. (b) Conventional reconstruction. (c) Sparsity-driven point-region enhanced reconstruction. (d) Sparsity-driven reconstruction with overcomplete Haar dictionary. (e) Proposed method with offline dictionary learning. (f) Proposed method with online dictionary learning.

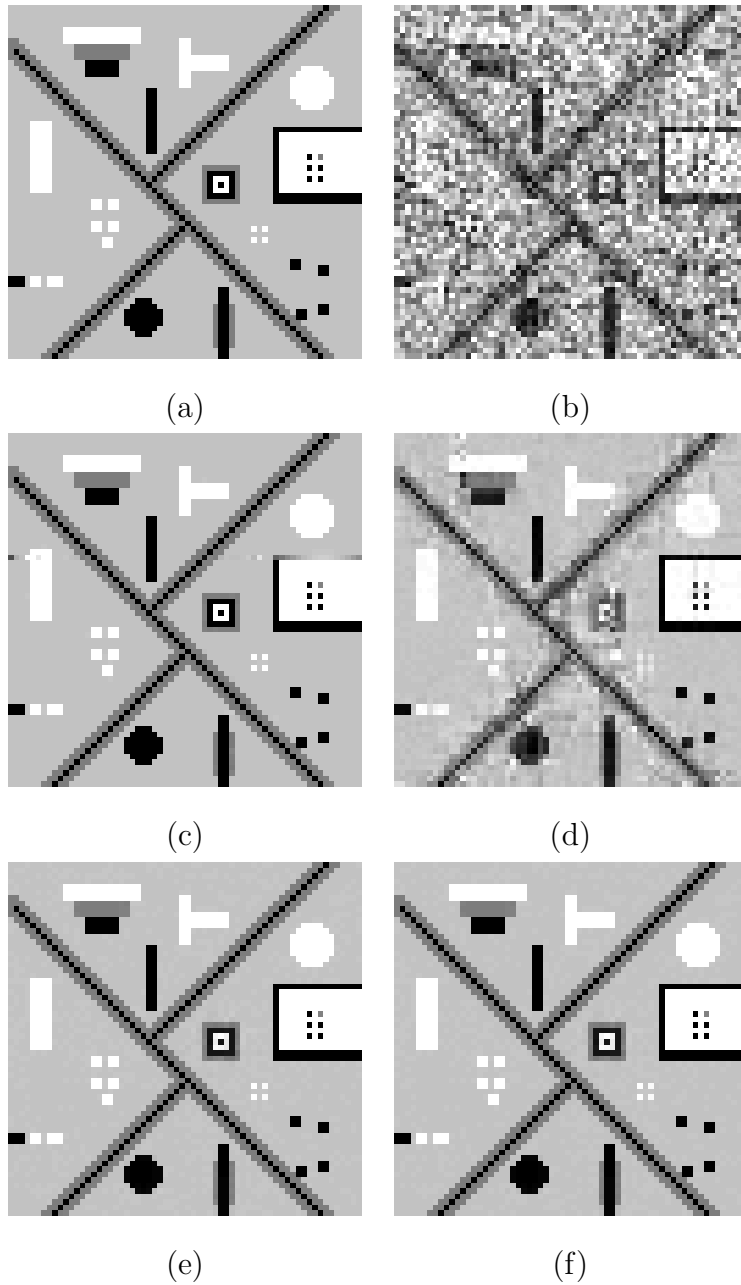


Figure 3.6: Results of the synthetic experiment with available data ratio $L = 0.8$. (a) Original scene. (b) Conventional reconstruction. (c) Sparsity-driven point-region enhanced reconstruction. (d) Sparsity-driven reconstruction with overcomplete Haar dictionary. (e) Proposed method with offline dictionary learning. (f) Proposed method with online dictionary learning.

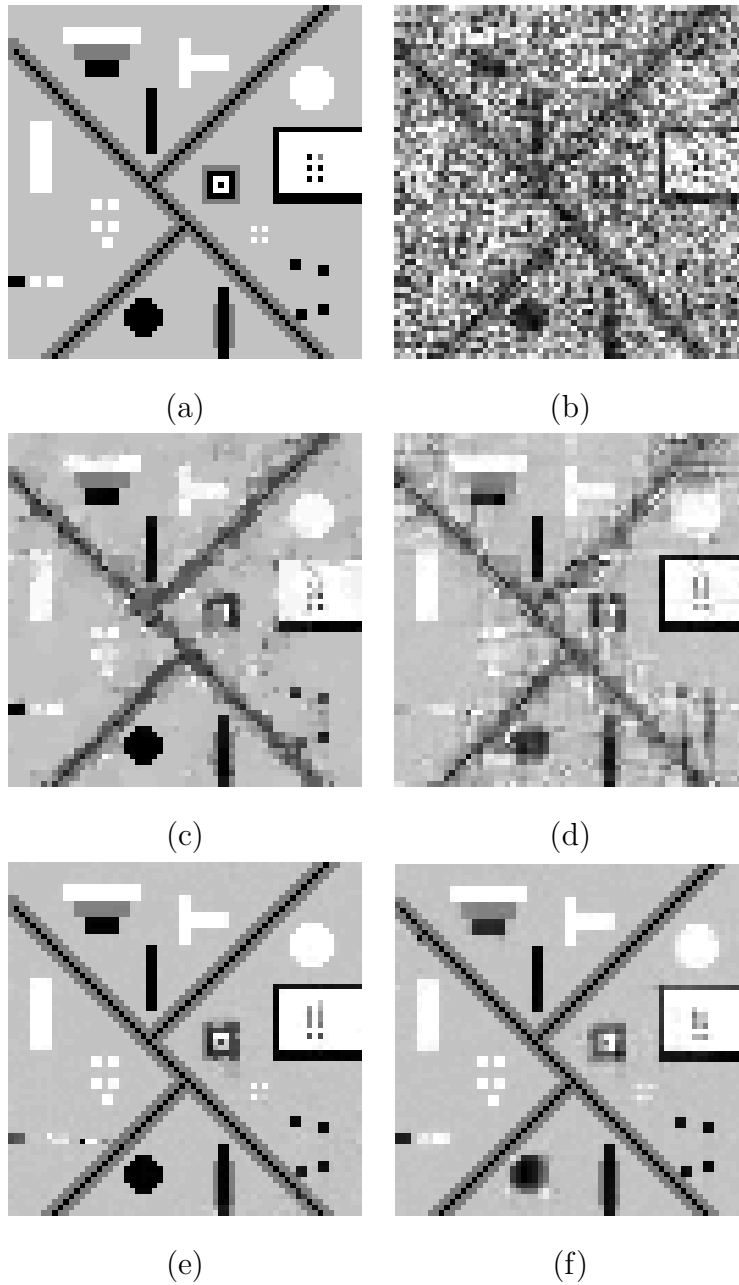


Figure 3.7: Results of the synthetic experiment with available data ratio $L = 0.7$. (a) Original scene. (b) Conventional reconstruction. (c) Sparsity-driven point-region enhanced reconstruction. (d) Sparsity-driven reconstruction with overcomplete Haar dictionary. (e) Proposed method with offline dictionary learning. (f) Proposed method with online dictionary learning.

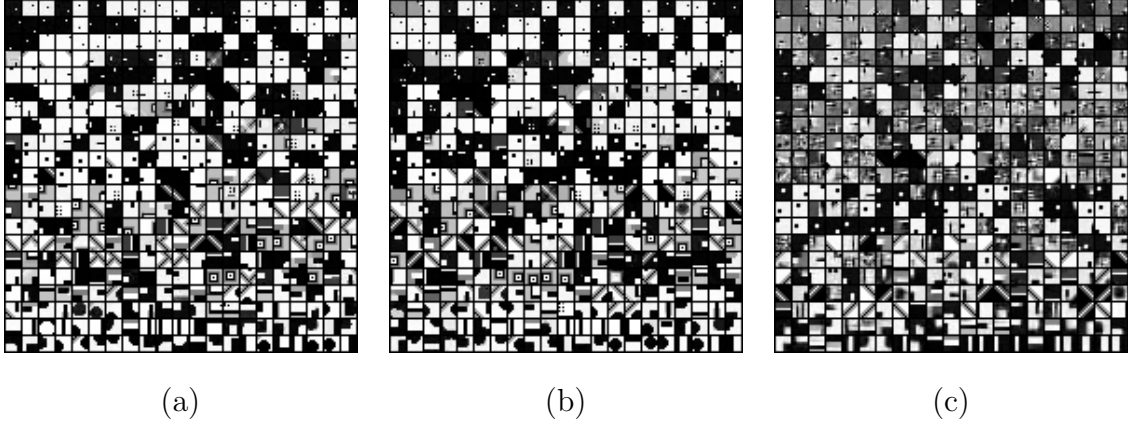


Figure 3.8: Online learned dictionaries for the synthetic test image with different L . (a) $L = 0.9$. (b) $L = 0.8$. (c) $L = 0.7$.

criterion is selected to be Minimum square error defined as:

$$MSE = \frac{1}{N} \left\| |f| - |\widetilde{f}| \right\| \quad (3.9)$$

where $|f|$ and $|\widetilde{f}|$ are the magnitudes of the original and reconstructed images. N is the total number of the pixels. We repeat this experiment for two different standard deviations of noise: $\sigma = 0.01$ and $\sigma = 1$ in order to assess the robustness of the methods to noise. For the two scenarios, reconstruction performances are shown in Figure 3.10. For the first case where $\sigma = 0.01$, both online and offline learning outperforms the other three methods. Wavelet-based reconstruction and point region enhanced non-quadratic regularization perform similarly. However, we can see that, as L decreases the former one provides better performance. For the second scenario where $\sigma = 1$ we see that, when L is between 0.6 and 1, our offline dictionary-based approach provides the best performance. However, the robustness of the point region enhanced non-quadratic regularization put itself forward.

3.2.2 Real SAR Scene Experiments

In this section we demonstrate the performance of our approach on the real SAR images obtained from the TerraSAR-X data set. Unlike the synthetic scene experiments for real SAR scenes a natural problem as mentioned in the beginning of this chapter

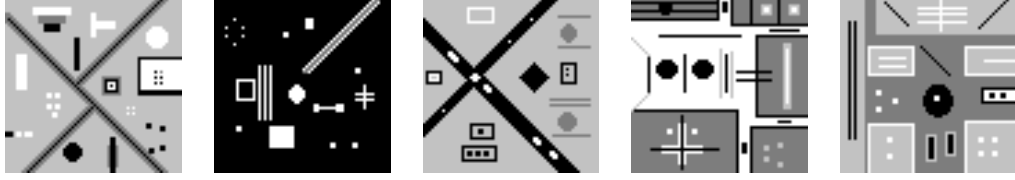
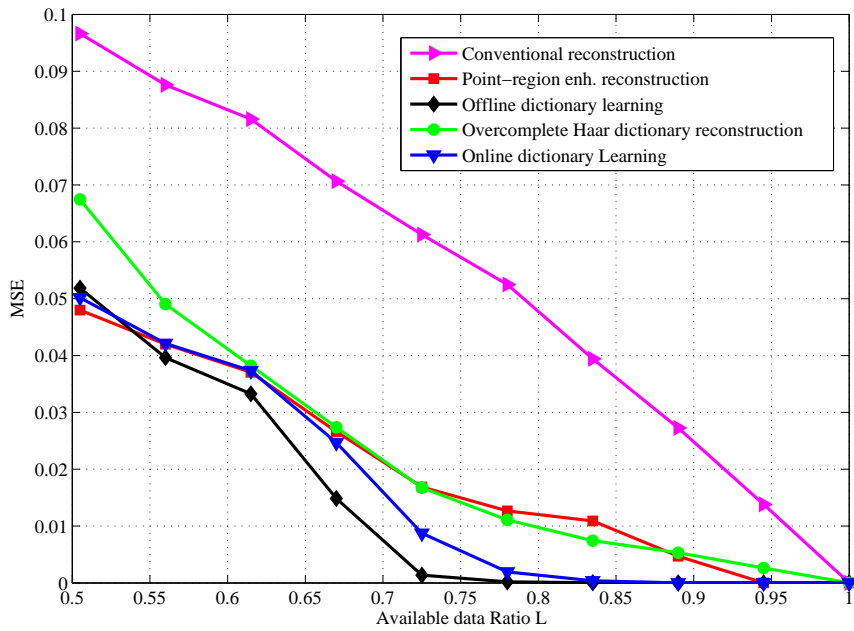


Figure 3.9: 5 synthetic test images used for the quantitative analysis.

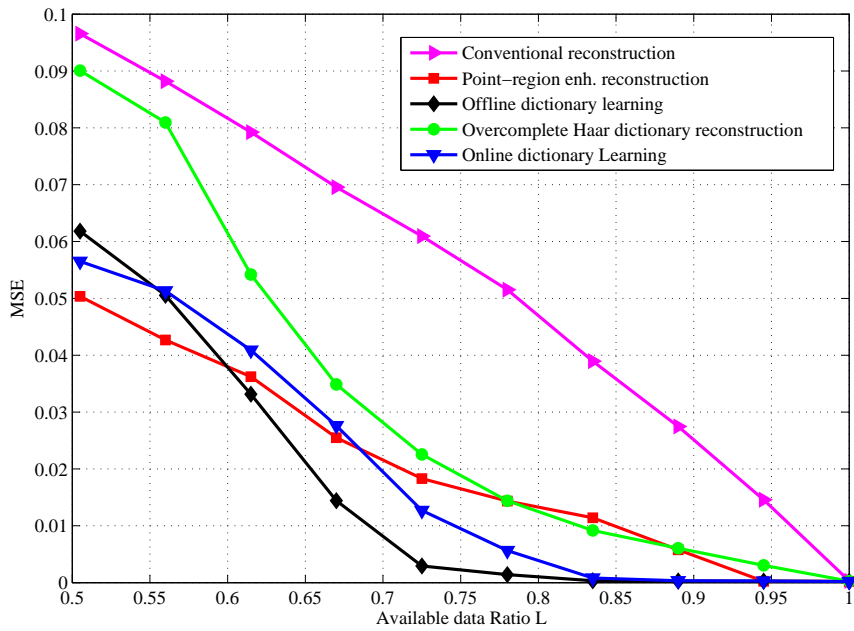
arises. Resolution of the SAR images is limited because of the SAR system bandwidth. Therefore, SAR images formed with conventional reconstruction suffer from sidelobes, and speckle. Thus, ground truth images does not exist in SAR imaging. Dictionaries learned from these SAR images may not be effective for reconstruction, because the learned dictionaries will also suffer from noise, speckle, and sidelobe. Remedy of this problem is applying a pre-processing stage for despeckling and denoising such as median filtering or learning from high resolution SAR images and applying it to SAR images with lower resolution. In this work, we preferred the latter one. We learn the dictionary from a data set and we test the proposed method with the test images with low resolution.

We used the Toronto data set provided by TerraSAR-X. These data have been collected in a spot-light mode. Range and azimuth resolutions are 3.75 and 3.69 meters respectively. The center frequency is 10 GHz. Polarization is HH. Approximate space between two consecutive pixels is 1.75 meters. In order to fit more information in one atom of the dictionary and reduce the size, we downsampled the data such that the pixel spacing to be 3.5 meters. For real SAR image experiments the dictionary size is selected to be 121×256 . In particular patch size is 11×11 so that each atom in the dictionary spans an area of $35 \times 35 m^2$. We select 100000 patches from SAR images. Training images are shown in Figure 3.11. DC component is removed from all the patches for efficiency. We run the K-SVD algorithm 300 times with sparsity level $T = 5$. Learned dictionary is shown in Figure 3.12.

As it is seen, the learned dictionary mostly captures the point scatterers and some edges. This is related to the intensity distribution of the SAR images. Natural SAR images usually have a background with low intensity and point scatterers with much



(a)



(b)

Figure 3.10: Results of the synthetic experiment with 5 test images. Different available data ratio values L vs MSE (a) Standard deviation of noise $\sigma = 0.01$. (b) $\sigma = 1$.

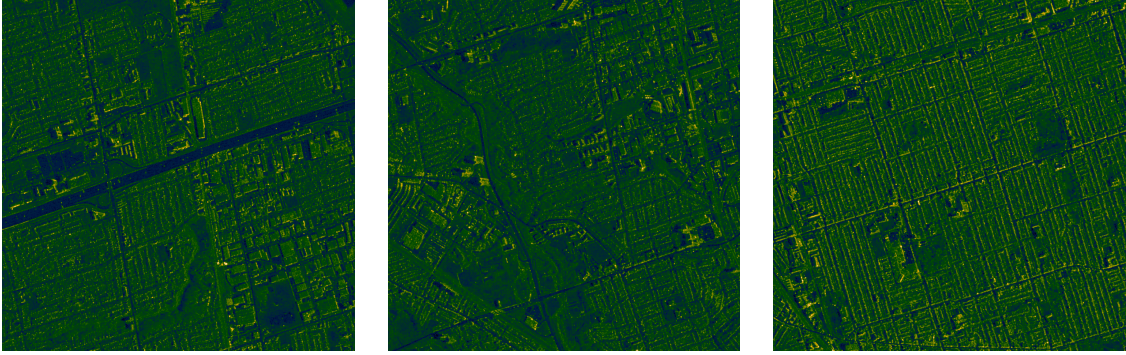


Figure 3.11: Training SAR images.

higher intensities. Thus, the learned dictionary is dominated by the point scatterers. It can be seen that, the bottom atoms of the dictionary represent the boundary regions between the foreground objects and the background.

However, learning a dictionary from the SAR image data set is questionable. Firstly, nonexistence of the true SAR image prevents the evaluation of the performance of the dictionary. Secondly, natural speckle and sidelobe of the SAR images affect the learning the dictionary. Therefore, before the reconstruction step, we visit another imaging problem which is image inpainting. We conduct an experiment for the performance of the learned dictionary over image inpainting. Note that our formulation can turn out to be an image inpainting formulation by changing the SAR forward model H to a pixel selection operator. For the sake of simplicity, rather than complex-valued data, we use only the magnitude of the SAR images. Therefore we can neglect the phase update step in our formulation. For this experiment, we removed 50% of the pixels of a SAR image and applied image inpainting with both DCT and learned dictionary. The results are shown in Figure 3.13. It can be seen that, the learned dictionary performs better than a predetermined DCT dictionary. This experiment reveals that, learned dictionaries and consequently our approach can be used for SAR image reconstruction.

We perform three distinct experiments with three distinct SAR images. For each of these experiments we have used a different L in order to demonstrate the performance of the reconstruction with respect to the percentage of available data. We compare our approach with conventional reconstruction, point-region enhanced regularization and

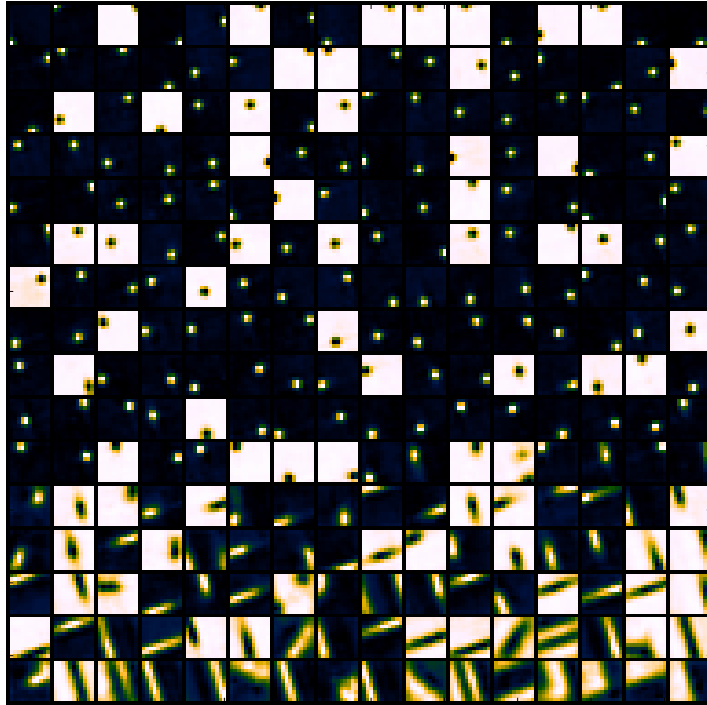
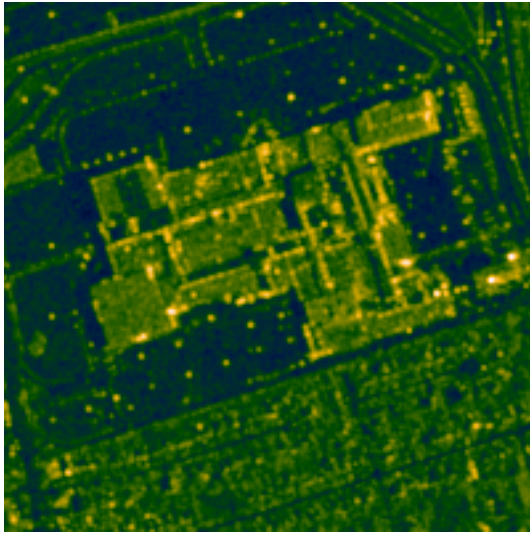
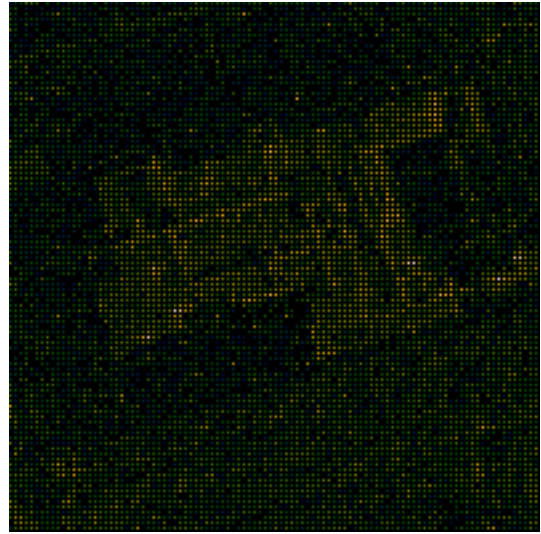


Figure 3.12: Learned dictionary from SAR images.

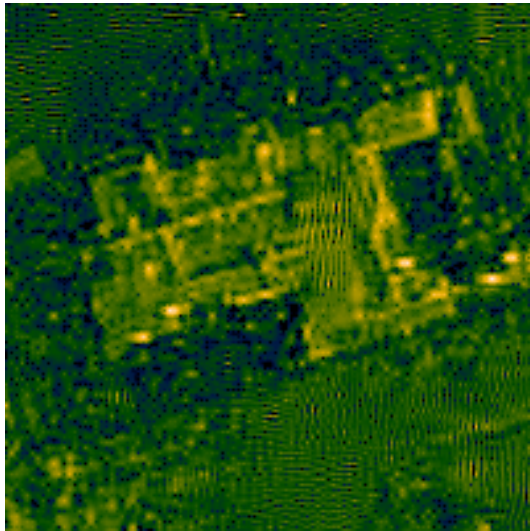
overcomplete DCT dictionary. For the first experiment we set $L \approx 0.8$ and $\sigma = 0.01$. We fixed the value of the σ for the SAR image reconstruction experiments. In Figure 3.14 we demonstrate the reconstruction results of all methods. We also provide magnified version of a particular region in the test image so as to analyze the reconstruction performances in detail. As we mentioned before, conventional reconstruction suffers from limited data. Point-region enhanced regularization performs fine but as we focus on the magnified version of the image, it can be seen that, this method causes some artifacts and suppresses small details. Overcomplete DCT dictionary fails to reconstruct the sidelobes effectively. We can see that, both offline and online learning provides successful reconstructions and as it is seen in the magnified image, these methods preserve edges effectively. However, since online learning learns the dictionary from the corrupted image patches, it also suffers from sidelobe and noise as in the case of DCT. We also demonstrate the reconstruction performance of the methods by reducing L further. In particular, reconstruction results are shown in Figure 3.15 and Figure 3.16 for $L \approx 0.7$ and $L \approx 0.66$. One important observation is, as we decrease L , online



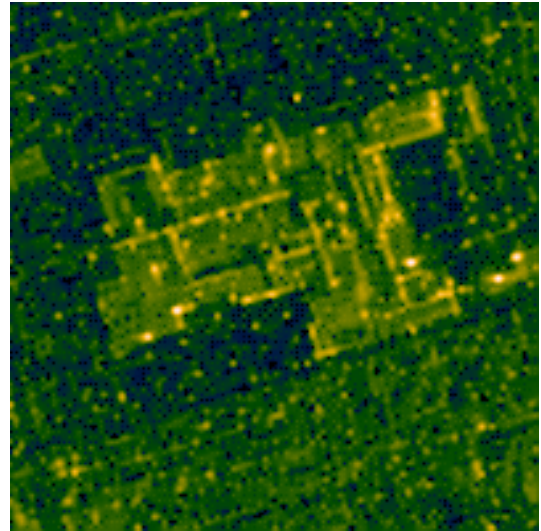
(a)



(b)



(c)



(d)

Figure 3.13: Result of inpainting of the SAR image with 50% missing pixels. (a) Original SAR scene. (b) %50 pixel missing data. (c) Inpainting result with overcomplete DCT. $MSE = 0.0002547$ (d) Inpainting result with learned dictionary. $MSE = 0.0001666$

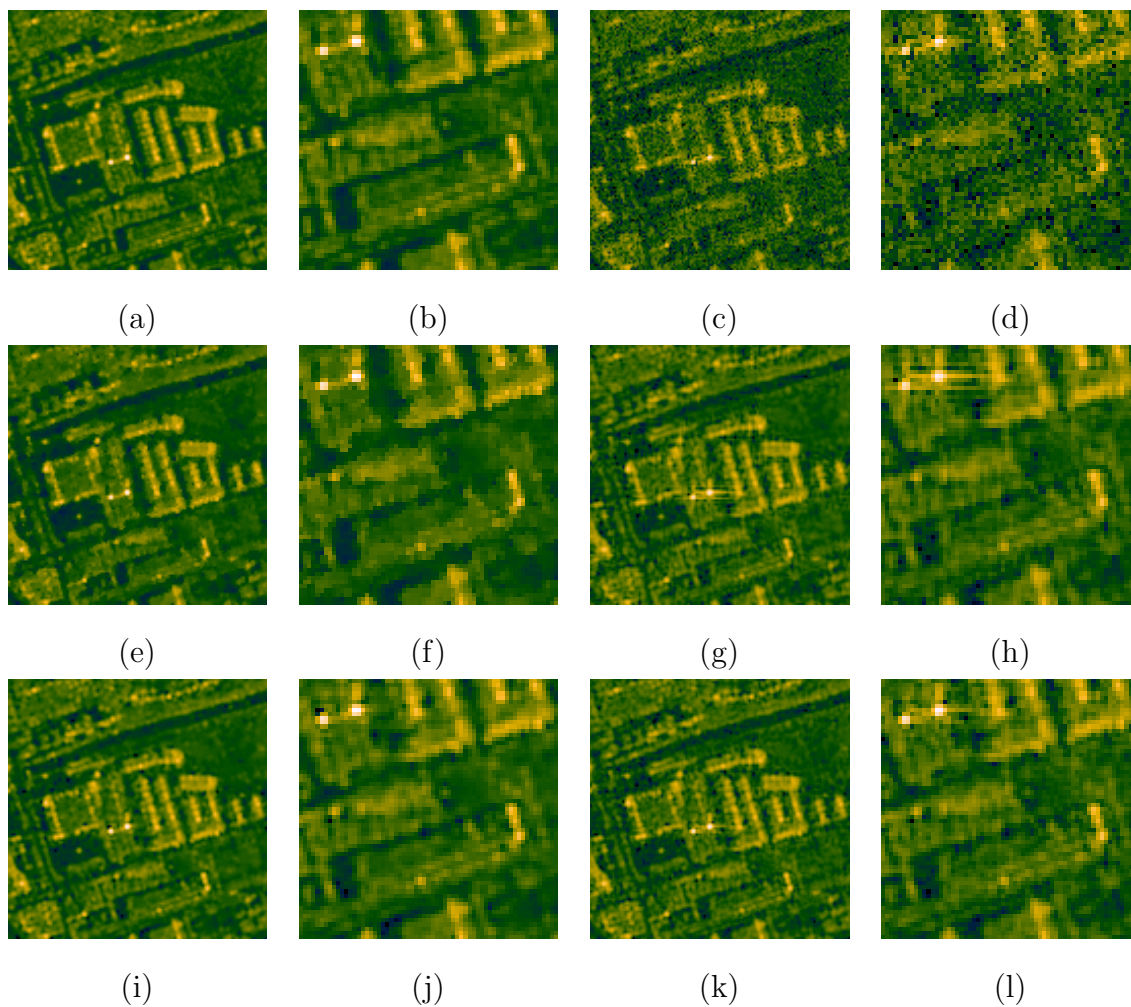


Figure 3.14: Result of the first experiment with $L \approx 0.8$. (a) Reconstructed image with full data. (b) Zoomed in version of a part of a. (c) Conventional reconstruction. (d) Zoomed in version of a part of c. (e) Image reconstructed with point-region enhanced regularization. (f) Zoomed in version of a part of e. (g) Image reconstructed with overcomplete DCT. (h) Zoomed in version of a part of g. (i) Image reconstructed with offline learning. (j) Zoomed in version of a part of i. (k) Image reconstructed with online learning. (l) Zoomed in version of a part of k.

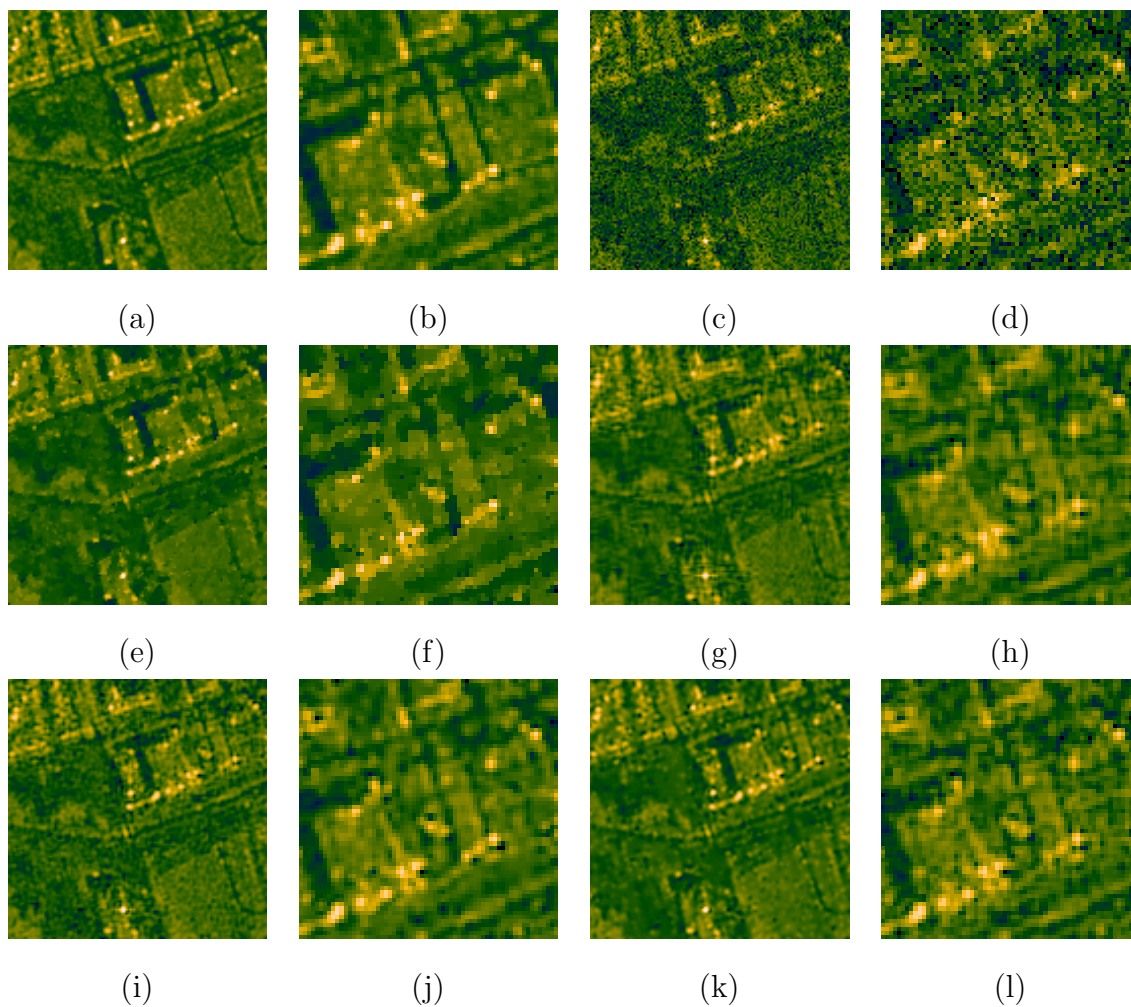


Figure 3.15: Result of the second experiment with $L \approx 0.7$. (a) Reconstructed image with full data. (b) Zoomed in version of a part of a. (c) Conventional reconstruction. (d) Zoomed in version of a part of c. (e) Image reconstructed with point-region enhanced regularization. (f) Zoomed in version of a part of e. (g) Image reconstructed with overcomplete DCT. (h) Zoomed in version of a part of g. (i) Image reconstructed with offline learning. (j) Zoomed in version of a part of i. (k) Image reconstructed with online learning. (l) Zoomed in version of a part of k.

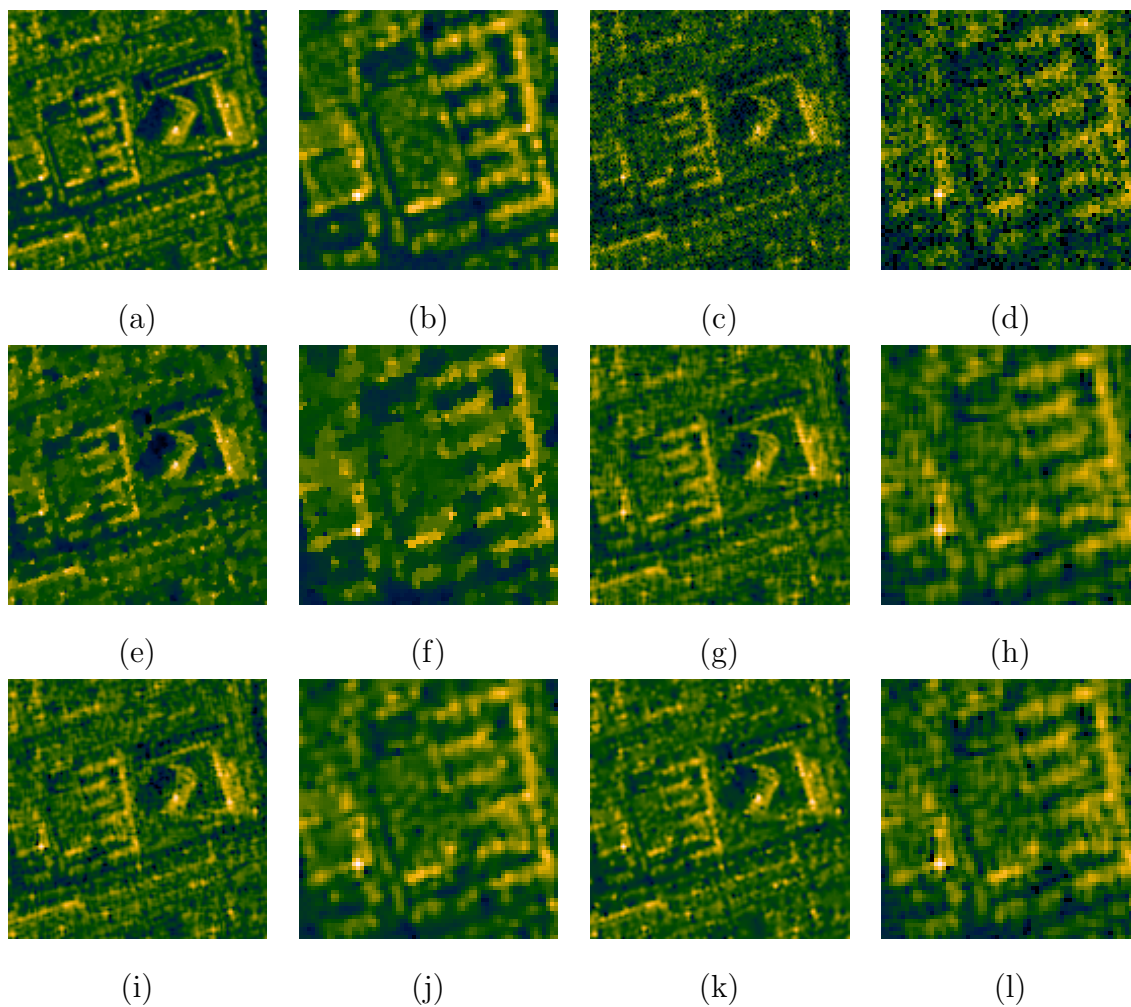


Figure 3.16: Result of the third experiment with $L \approx 0.66$. (a) Reconstructed image with full data. (b) Zoomed in version of a part of a. (c) Conventional reconstruction. (d) Zoomed in version of a part of c. (e) Image reconstructed with point-region enhanced regularization. (f) Zoomed in version of a part of e. (g) Image reconstructed with overcomplete DCT. (h) Zoomed in version of a part of g. (i) Image reconstructed with offline learning. (j) Zoomed in version of a part of i. (k) Image reconstructed with online learning. (l) Zoomed in version of a part of k.

Table 3.2: Reconstruction performance of the methods on real SAR scenes in terms of MSE.

Method	$L = 0.9$	$L = 0.85$	$L = 0.80$	$L = 0.71$	$L = 0.66$	$L = 0.63$
Conventional	0.00066	0.00107	0.00147	0.00201	0.00232	0.00254
PR enh. reg.	0.00006	0.00016	0.00032	0.00069	0.00095	0.00112
DCT	0.00008	0.00019	0.00044	0.00087	0.00111	0.00124
Offline learning	0.00003	0.00007	0.00017	0.00052	0.00081	0.0009
Online learning	0.00003	0.00011	0.00030	0.00073	0.00100	0.00116

learning suffers greater than offline learning. The reason is obvious. As the images are corrupted more, learning a sparsifying dictionary from these corrupted images becomes more difficult.

We also provide some quantitative result of the reconstruction performances of the methods in Table 3.2. We average MSE of the reconstruction over 3 experiments. We used reconstructed image with full data ($L = 1$) as ground truth image. Note that, the performance of the online learning is diminishing more than offline learning since online learning is harder when L is small.

Chapter 4

Low-rank Sparse Decomposition Framework for SAR Imaging

In this chapter, we integrate low-rank sparse decomposition (LRSD) into the SAR image reconstruction problem. We formulate the optimization problem and propose an iterative solution. We present the effectiveness of the proposed method on synthetic and real SAR scenes.

4.1 Proposed LRSD-based Framework

Decomposing an image or signal into two or more parts has found use in many image analysis problems such as background subtraction, denoising and segmentation. These methods are used for supporting later stages of analysis such as object detection and recognition. Therefore, the accuracy of the decomposition affects the performance of these inference or decision making tasks. Decomposing sparse objects and the background of the scene is one of the typical problems for the above mentioned applications. Recently, there has been interest in this decomposition problem, where the background of the scene is assumed to be a low-rank matrix. Besides, recent pieces of work have reported that under very mild conditions, decomposition of low-rank and sparse components (LRSD) from partial or corrupted measurements is possible [54, 9]. The LRSD model has been used in many applications problem including face recognition [16] and background subtraction [7]. LRSD has also been used as a prior term in inverse problems in imaging, such as medical image reconstruction [35, 58].

SAR imaging applications also involve the above mentioned interpretation tasks

such as object recognition, and object tracking. In general, SAR image formation and further image analysis are performed in a decoupled fashion. Interpretation methods are applied to the SAR image after SAR image formation has been completed. However, this situation has one disadvantage. The image formation algorithm may produce an unsuitable image for interpretation methods since the higher level objectives of the interpretation stage are not used in the formation process. Therefore, a SAR image that is potentially better suited to the higher-level inference goals might be formed by adding information about these objectives into the SAR imaging problem.

In this work, we integrate the LRSD framework into the SAR imaging problem. The proposed method has two advantages. Firstly, we decompose sparse components and low-rank background in the SAR scene while reconstructing the SAR image. Therefore, for SAR applications, the proposed method provides two additional images along with a composite SAR image: a sparse image which contains sparse objects on the scene and the low-rank background image. Secondly, the proposed method may essentially perform partial image analysis during the reconstruction phase, if for example the application involves segmentation of the sparse objects, or subtraction of the background from the SAR scene.

In order to exploit the LRSD framework in SAR image reconstruction, the vectorized form of SAR image $f \in \mathbb{C}^N$ should be converted to the matrix form. The image form of this vector where size of the image is $\sqrt{N} \times \sqrt{N}$ can be used as a matrix. However, low-rank assumption of a complete SAR image is unrealistic and may provide inefficient results. Therefore, we use a patch-based method for constructing the matrix form of the SAR image. Let R be the linear operator that constructs a patch-based matrix from the image. Image patches $f_i \in \mathbb{C}^{\sqrt{n} \times \sqrt{n}}$ are obtained from the image by using a sliding window starting from top-left of the image to the bottom-right. Note that, for the sake of simplicity and with a slight abuse of notation, we use f_i for both the matrix and the vectorized forms of the image patches. Vectorized form of these patches form columns of the patch-based matrix. The patch-based matrix $F \in \mathbb{C}^{n \times K}$

has the form of

$$F = \begin{bmatrix} | & | & & & | \\ f_1 & f_2 & \cdot & \cdot & f_K \\ | & | & & & | \end{bmatrix} \quad (4.1)$$

where K depends on sliding distance and size of the patches. This matrix can be deconstructed to recover the original image. Note that if the sliding distance is smaller than \sqrt{n} , there will be overlapping patches and F will contain repeated entries for the same pixels. We take mean of these values in the process of deconstructing F to reconstruct the image f . This patch-based method has been used in [25] for small target detection.

As discussed in Chapter 3, SAR scene exhibits random phase, which should be taken into account in imposing sparsity and low-rank structure to the complex-valued SAR scene. Thus, we represent the magnitude of the SAR image with this matrix F such that $F = R(|f|)$. The reconstruction process can be expressed as $|f| = R^*(F)$. Let B and S be the patch-based image for low-rank background and sparse part respectively. Thus, SAR observation model can be expressed as

$$g = H\Theta R^*(B + S) + n \quad (4.2)$$

Using this notation, the proposed LRSD-based SAR imaging problem can be expressed as follows:

$$\begin{aligned} \left\{ \widehat{B}, \widehat{S}, \widehat{\Theta} \right\} &= \arg \min_{B, S, \Theta} \|g - H\Theta R^*(B + S)\|_2^2 + \lambda_b \|B\|_* + \lambda_s \|S\|_1 \\ s.t. \quad &|\Theta_{(i,i)}| = 1 \quad \forall i \end{aligned} \quad (4.3)$$

where the diagonal matrix Θ contains the exponentiated phase of the reflectivity field, λ_b and λ_s are regularization parameters, $\|\cdot\|_*$ is the nuclear norm as described in Chapter 2, the $\|\cdot\|_1$ is l_1 norm. The first term enforces the data fidelity, the second term enforces the matrix to be low-rank and the third term enforces sparsity. It is not straightforward to solve this problem with current LRSD methods since it involves the data fidelity term. Therefore, we use variable splitting method by introducing a variable F such

that $F = B + S$. Constraint optimization problem takes the form of

$$\begin{aligned} \{\widehat{F}, \widehat{B}, \widehat{S}, \widehat{\Theta}\} &= \arg \min_{F, B, S, \Theta} \|g - H\Theta R^*(F)\|_2^2 + \lambda_b \|B\|_* + \lambda_s \|S\|_1 \\ \text{s.t.} \quad & F = B + S \\ \text{s.t.} \quad & |\Theta_{(i,i)}| = 1 \quad \forall i \end{aligned} \tag{4.4}$$

In the image domain, S represents the image that contains sparse components, B represents the approximately low-rank background image, and F represents the composite image. The proposed method enforces the low-rank constraint to the patches of the image. This enforces that small regions of the background are correlated. The augmented Lagrangian form of this problem can be expressed as follows:

$$\begin{aligned} L(F, B, S, \Theta, Z) &= \arg \min \|g - H\Theta R^*(F)\|_2^2 + \lambda_b \|B\|_* + \lambda_s \|S\|_1 \\ &\quad + \langle Z, F - B - S \rangle + \frac{\beta}{2} \|F - B - S\|_F^2 \\ \text{s.t.} \quad & |\Theta_{(i,i)}| = 1 \quad \forall i \end{aligned} \tag{4.5}$$

where Z is the Lagrange multiplier, and $\beta > 0$ penalizes the violation of the constraint. We use alternating direction method of multipliers (ADMM) for the solution of the problem. In particular, we introduced an auxiliary variable F in order to solve B and S separately. We minimize the problem over one variable while keeping other variables fixed. ADMM simplifies the problem hence it allows to take the advantage of the separable structures of B and S as it is expressed in LRSD schemes.

4.2 Solution of the Optimization Problem

There are 5 different variables to be solved for F, B, S, Z, Θ . For each iteration, each of these parameters is solved for by keeping other variables fixed by using ADMM. Below, we describe the process of updating each of these variables for a generic $(k + 1)^{st}$ iteration.

Solution of the Sparse Matrix $S^{(k+1)}$

This step solves for the sparse matrix S while keeping the other variables fixed. Dropping the constant terms, the subproblem of interest takes the form of

$$S^{(k+1)} = \arg \min_S \lambda_s \|S\|_1 + \langle Z^{(k)}, F^{(k)} - B^{(k)} - S \rangle + \frac{\beta}{2} \|F^{(k)} - B^{(k)} - S\|_F^2 \quad (4.6)$$

This problem is in a form that it equivalent to the well-known LASSO problem and can be solved via soft thresholding as discussed in Section 2.5.4. Recall that the soft thresholding operator can be expressed as follows:

$$\tilde{C}_\epsilon(S) = \begin{cases} S - \epsilon & \text{if } S > \epsilon \\ S + \epsilon & \text{if } S < -\epsilon \\ 0 & \text{otherwise} \end{cases} \quad (4.7)$$

Therefore solution of the problem is $S^{(k+1)} = \tilde{C}_{\frac{\lambda_s}{\beta}}(F^{(k)} - B^{(k)} + \frac{Z^{(k)}}{\beta})$.

Solution of the Low-rank Matrix $B^{(k+1)}$

In this step, we update the low-rank matrix B . The subproblem for this step is

$$B^{(k+1)} = \arg \min_B \lambda_b \|B\|_* + \langle Z^{(k)}, F^{(k)} - S^{(k+1)} - B \rangle + \frac{\beta}{2} \|F^{(k)} - S^{(k+1)} - B\|_F^2 \quad (4.8)$$

This subproblem involves nuclear norm minimization and as we discussed in Section 2.5.2, its subgradient computation can be done through singular value thresholding. In particular the soft thresholding operator is applied on the singular values of the matrix. The solution of this problem can be expressed as follows:

$$S^{(k+1)} = U_k \tilde{C}_{\frac{\lambda_b}{\beta}}(\Sigma_k) V_k^T \quad (4.9)$$

where $U_k \Sigma_k V_k^T$ is the singular value decomposition of the matrix $F^{(k)} - S^{(k+1)} + \frac{Z^{(k)}}{\beta}$. Both singular value thresholding and soft thresholding are element-wise operations. Thus, these operations are computationally efficient except for the computation of the singular value decomposition.

Solution of the Patch-based Matrix $F^{(k+1)}$

In this step, we update the patch-based matrix F for the following subproblem.

$$F^{(k+1)} = \arg \min_F \left\| g - H\Theta^{(k)}R^*(F) \right\|_2^2 + \left\langle Z^{(k)}, F - S^{(k+1)} - B^{(k+1)} \right\rangle + \frac{\beta}{2} \left\| F - S^{(k+1)} - B^{(k+1)} \right\|_F^2 \quad (4.10)$$

This subproblem is quadratic and can be solved analytically. Taking the derivative with respect to F and equating it to zero gives the following equation.

$$\left(2 \left(H\Theta^{(k)}R^* \right)^H \left(H\Theta^{(k)}R^* \right) + \beta I \right) F^{(k+1)} = \left(2 \left(H\Theta^{(k)}R^* \right)^H g + \beta \left(B^{(k+1)} + S^{(k+1)} \right) - Z^{(k)} \right) \quad (4.11)$$

We solve this problem with a few conjugate gradient steps.

Solution of the Phase Matrix $\Theta^{(k+1)}$

For this solution we introduce a vector p consisting the diagonal elements of the phase matrix Θ . The corresponding subproblem is

$$\hat{p} = \arg \min_p \left\| g - H\tilde{B}p \right\|_2^2 + \lambda_p \sum_{i=1}^N (|p_i| - 1)^2 \quad (4.12)$$

where \tilde{B} is the diagonal matrix consists of elements of $R^*(F^{(k+1)})$. This problem is similar to the phase update step involved in our dictionary learning-based image formation algorithm described in Section 3.1.2. We solve this problem in the same way.

Lagrange Multiplier Update and Continuation

We update the Lagrange multiplier Z at each iteration with step size β . In particular, Z is updated as follows:

$$Z^{(k+1)} = Z^{(k)} + \beta(F^{(k+1)} - B^{(k+1)} - S^{(k+1)}) \quad (4.13)$$

Note that when value of β is high, the ALM form of the optimization problem approaches to the constrained version of the problem in (4.4). However, large value of β leads to slow convergence of the algorithm. Thus, we use a continuation strategy for β . In particular, we start with small β and at each iteration we increase β slowly. These iterative steps are run until the convergence criterion $\frac{\left\| |F|^{(k+1)} - |F|^{(k)} \right\|_F}{\left\| |F|^{(k)} \right\|_F} < \delta_x$ is satisfied. The steps of the proposed method are summarized in Algorithm 5.

Algorithm 5 Structure of the Proposed Algorithm

1. Input: $g, H, \delta_x, \delta_p, \lambda_b, \lambda_s \lambda_p$

2. Initialization: $F^{(0)} = R(|H^H g|), p_0 = e^{j\phi(H^H g)}, S^{(0)} = 0, B^{(0)} = F^{(0)}, Z^{(0)} = 0, k = 0$

while Stopping criteria is not satisfied **do**

3. Sparse Matrix Update:

$$S^{(k+1)} = \tilde{C}_{\frac{\lambda_s}{\beta}}(F^{(k)} - B^{(k)} + \frac{Z^{(k)}}{\beta})$$

4. Low-rank Matrix Update:

$$U_{k+1} \Sigma_{k+1} V_{k+1}^T = F^{(k)} - S^{(k+1)} + \frac{Z^{(k)}}{\beta}$$

$$B^{(k+1)} = \tilde{C}_{\frac{\lambda_b}{\beta}}(\Sigma_{k+1})$$

6. Phase Update

Update $\Theta^{(k+1)}$ by solving (4.12) with CG until $\frac{\|p^{(n+1)} - p^{(n)}\|}{\|p^{(n)}\|} < \delta_p$ is satisfied.

7. Patch-based Matrix Update:

Solve (4.11) and update $F^{(k+1)}$

8. Multiplier Update:

$$Z^{(k+1)} = Z^{(k)} + \beta(F^{(k+1)} - B^{(k+1)} - S^{(k+1)})$$

$$\beta = \rho\beta$$

$$k = k + 1$$

end while

4.3 Experimental Results

In this section we present experimental results evaluating the performance of the proposed method using both synthetic scenes and real SAR scenes from the TerraSAR-X dataset. We provide quantitative results on the synthetic scene experiments. In the experiments we used a band-limited Fourier transform as our forward model H . We display the sparse part, the low-rank background part and the composite image produced by the proposed approach. We compare the performance of the proposed method with conventional reconstruction methods and point-region enhanced regularization method [14] with respect to mean squared error (MSE) as we did in the previous chapter.

4.3.1 Synthetic Scene Experiments

We use a 64×64 synthetic scene for the first set of experiments. We compose a synthetically constructed sparse scene and a low-rank background scene. The sparse and low-rank background parts used for this experiment along with the composite scene are presented in Figure 4.1. Note that, the composite image can be seen as man-made metallic scatterers on natural terrain. Uniformly distributed random phase between $[-\pi, \pi]$ is added to the composite image. We add Gaussian noise to the phase history data generated using a band-limited Fourier transform operator as mentioned above.

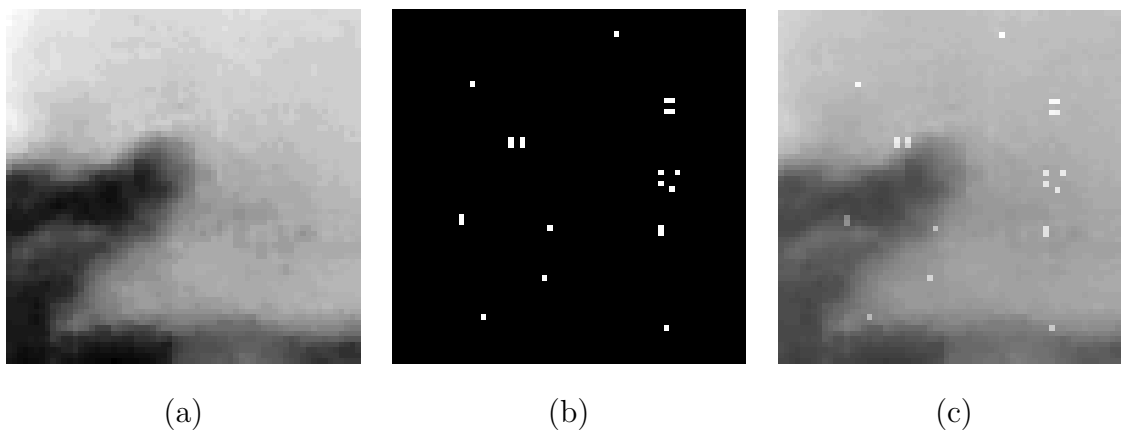


Figure 4.1: Synthetically constructed test Image. (a) Low-rank background part. (b) Sparse part. (c) Composite image.

Table 4.1: Reconstruction performance of the methods on synthetic SAR scenes in terms of MSE.

Method	$L = 0.88$	$L = 0.76$	$L = 0.66$
Conventional	0.02087	0.04174	0.05666
PR enhanced reg.	0.00004	0.00014	0.00214
Proposed method	0.00005	0.00012	0.00055

We aim to reconstruct an estimate of the low-rank background, the sparse part and the composite image based on these phase histories. We present synthetic scene experiment results for three different values of L . Recall that L is the percentage of the available data. We show the performance of the proposed method, conventional reconstruction method and point-region enhanced reconstruction. The results of this experiment are shown in Figure 4.2. For the first two results where $L = 0.88$ and $L = 0.76$, the proposed method decomposes the sparse and the low-rank parts of the scene accurately. Hence it provides an accurate composite image. Note that, the conventional approach does not produce sufficiently accurate results for visual or automated interpretation of the scene. Proposed method provides accurate sparse part and low-rank background for the interpretation. As an example, if the task of the SAR application is detection of these sparse parts, the sparse part from the proposed method can be used for such analysis. When $L = 0.66$ the performance of the proposed method in terms of decomposing the sparse and low-rank background components deteriorates. However it still provides a good estimate for the low-rank background. The proposed method provides comparable reconstruction results with respect to point-region enhanced regularization. Note that, point-region enhanced reconstruction suffers from artifacts and it fails to provide an efficient reconstruction for the background of the image when $L = 0.66$. One advantage of the proposed method is that it also provides sparse and low-rank background images since it decomposes sparse and background components of the image. We provide the corresponding MSE results for this experiment in Table 4.1.

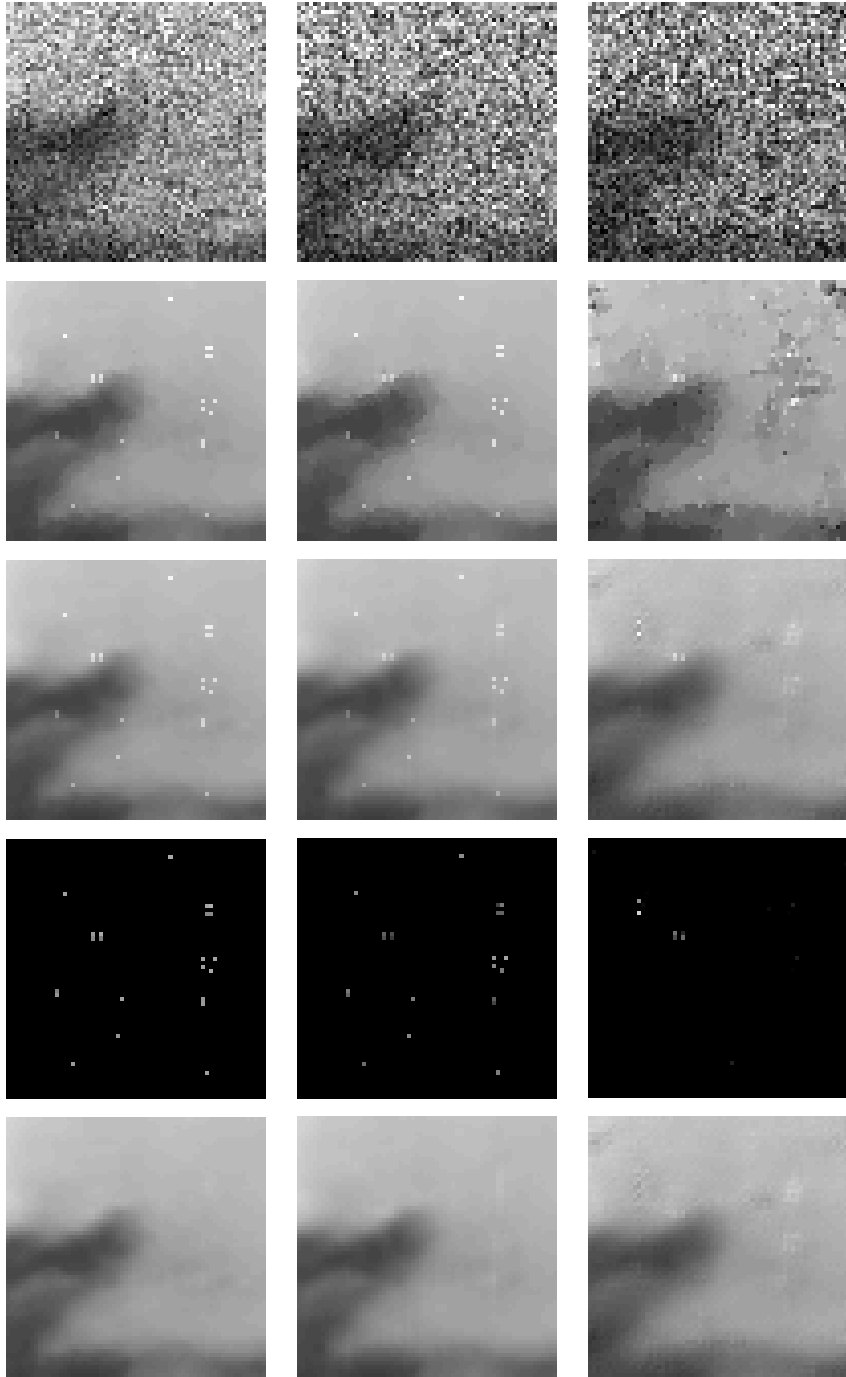


Figure 4.2: Result of the first experiment with $L = 0.88, 0.76, 0.66$ for the first, second and third columns respectively. Conventional reconstruction (first row). Point-region enhanced reconstruction (second row). The composite image produced by the proposed approach (third row). The sparse component produced by the proposed approach (fourth row). The low-rank component produced by the proposed approach (fifth row).

4.3.2 Real SAR Scene Experiments

We now present experimental results on real SAR scenes obtained from the TerraSAR-X dataset. In the first experiment we use SAR data that have been collected in a staring spotlight mode with 0.85 m range and 0.35 m azimuth resolution. We use 128×128 SAR data for the experiments. The test image contains a water treatment facility in Egypt. Note that this image contains repeating objects. For an appropriate selection of patch size, columns of the patch-based matrix will be similar to each other implying that patch-based matrix is low-rank. Therefore, the patch-based low-rank component in our approach enforces that small regions in the image are similar. Thus, this test image is a good candidate for the LRSF framework. Available data ratio is set to $L \approx 0.9$ for this experiment. Reconstruction results are shown in Figure 4.3. Proposed method appears to effectively decompose the background and sparse part of the SAR scene and it provides similar reconstruction result with point-region enhanced regularization. The sparse part contains the point scatterers around the repeating objects and the background part enhances these repeating objects. Note that the background part can be more useful for SAR imaging analysis such as counting these repeating objects in the image since it does not involve sparse point scatterers.

In the second experiment, we have used SAR data collected in a spotlight mode with 3.75 m range and 3.69 m azimuth resolutions. Image size is 128×128 . The test image covers a region in Toronto including roads and small houses. Note that, these structures exhibit similarity as in the case for the first experiment hence low-rank background can be enforced on these structures. We reduce available data ratio to $L \approx 0.77$ for the second experiment. Reconstruction results are shown in Figure 4.4. The proposed method captures sparse scatterers in the sparse part and low-rank structures are well preserved in the low-rank background image as compared to the point-region enhanced regularization and conventional methods. We also provide the zoomed-in version of this experiment in Figure 4.5. Note that, the background part preserved the road and small repeating objects on the image.

For the third experiment we used an image of a park in Toronto. The SAR parameters are identical to those of the second experiment. Image size is 100×100 . This image

contains strong scatterers and a weak background structure in terms of the intensity. We aim to represent these weak textures in the low-rank background part and strong scatterers in the sparse part. Reconstruction results are shown in Figure 4.6. Available data ratio for this experiment is set to $L \approx 0.71$. Conventional method suffers from the noise and speckle. Point-region enhanced regularization preserves strong point scatterers. However, since point-region enhanced regularization method is a sparsity-driven method, it suppresses weak textures in the background. Proposed method preserves these weak texture in the background part and strong scatterers in the sparse part. Therefore, for SAR imaging applications where the background texture is required, proposed method provides an efficient reconstructed composite image along with the sparse part and the low-rank background part.

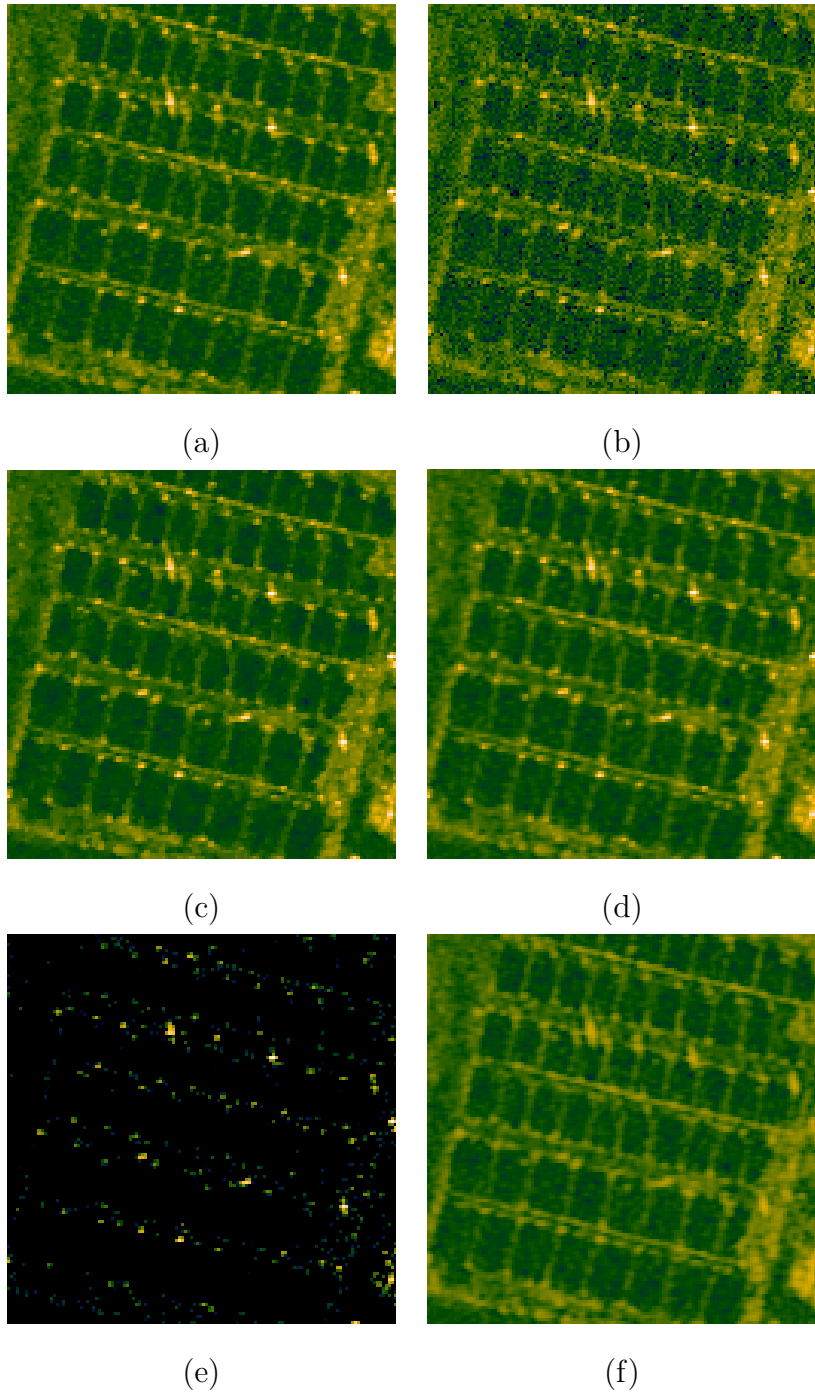


Figure 4.3: Result of the first experiment with $L \approx 0.90$. (a) Reconstructed image with full data. (b) Conventional reconstruction. (c) Image reconstructed with point-region enhanced regularization. (d) Proposed method: Composite image. (e) Proposed method: sparse image. (f) Proposed method: low-rank image.

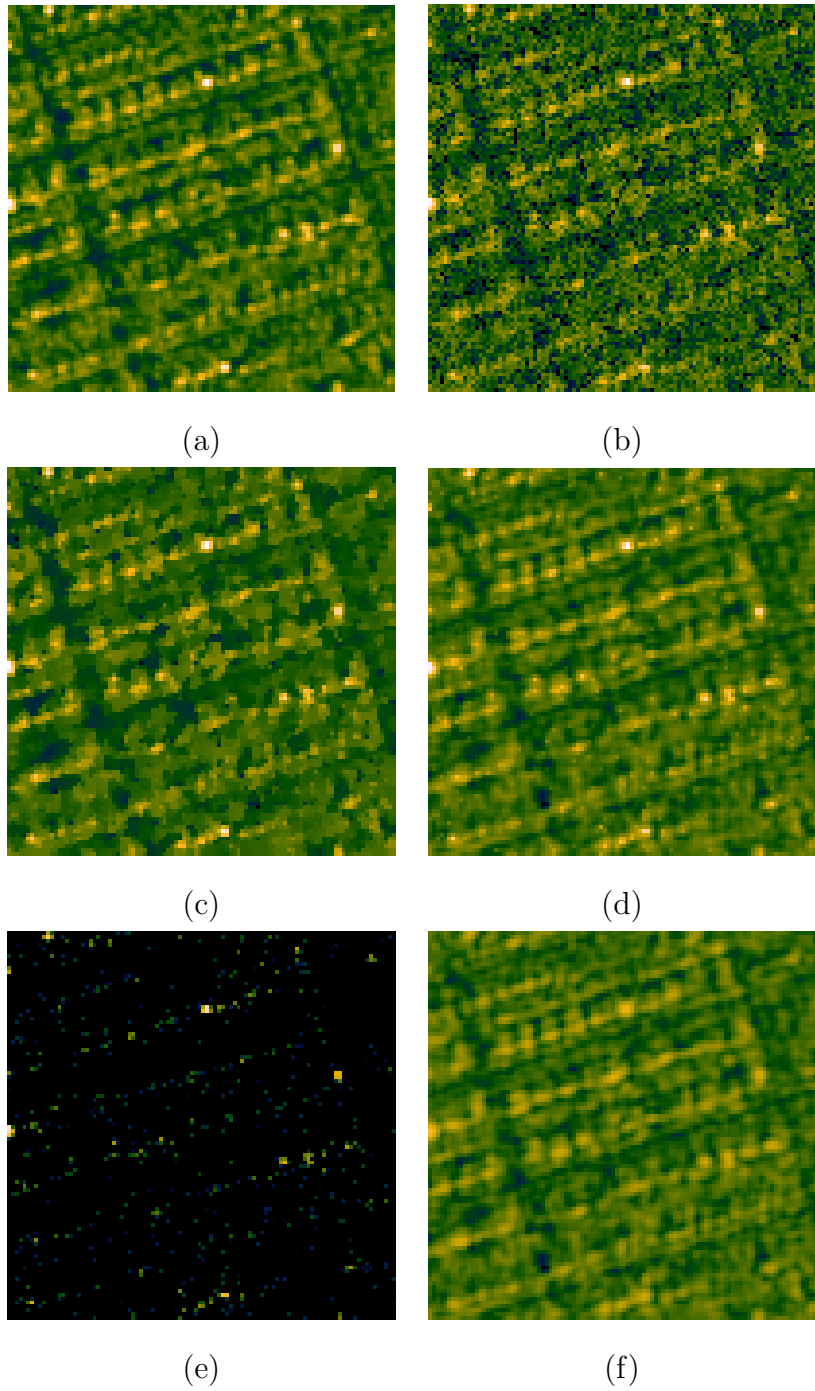


Figure 4.4: Result of the second experiment with $L \approx 0.77$. (a) Reconstructed image with full data. (b) Conventional reconstruction. (c) Image reconstructed with point-region enhanced regularization. (d) Proposed method: Composite image. (e) Proposed method: sparse image. (f) Proposed method: low-rank image.

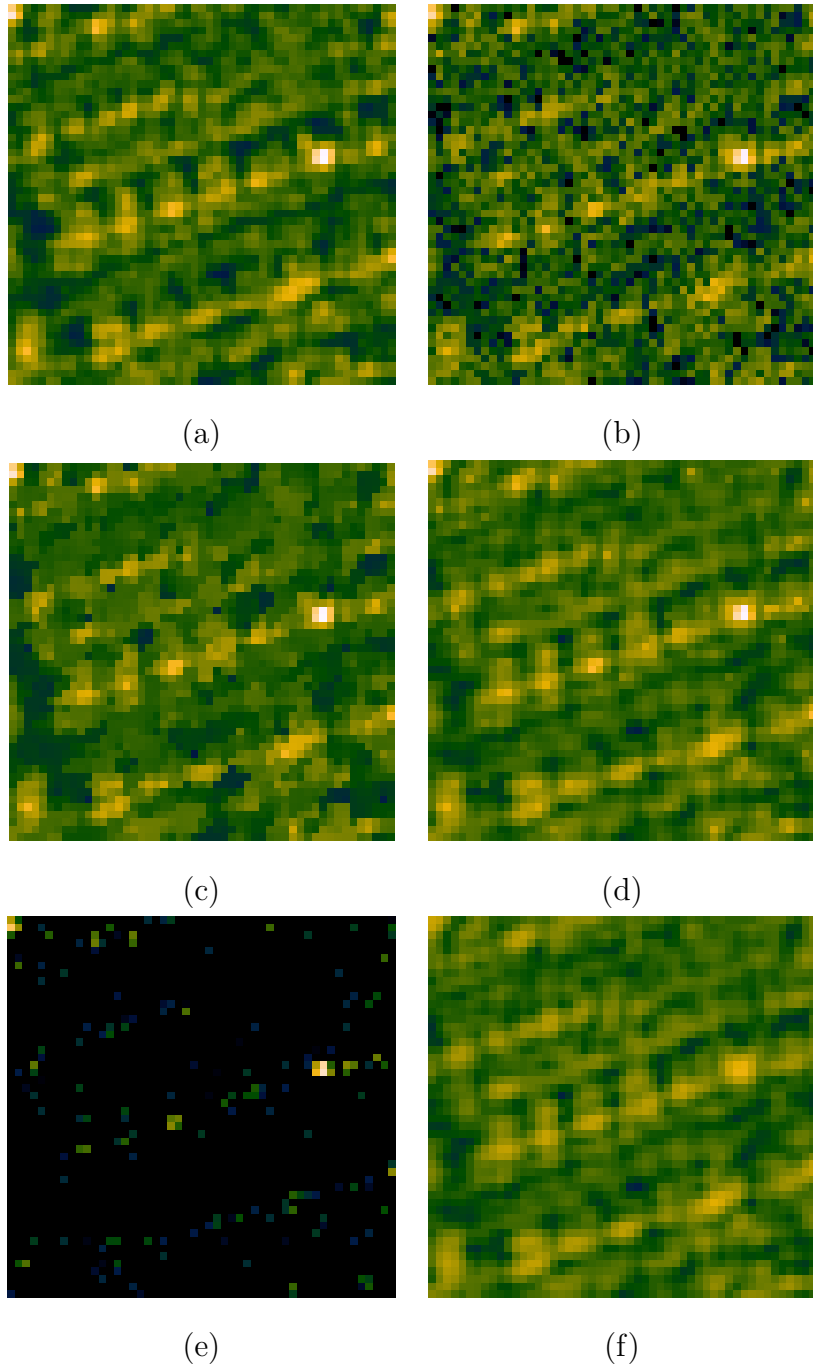


Figure 4.5: Zoomed in version of the second experiment. (a) Reconstructed image with full data. (b) Conventional reconstruction. (c) Image reconstructed with point-region enhanced regularization. (d) Proposed method: Composite image. (e) Proposed method: sparse image. (f) Proposed method: low-rank image.

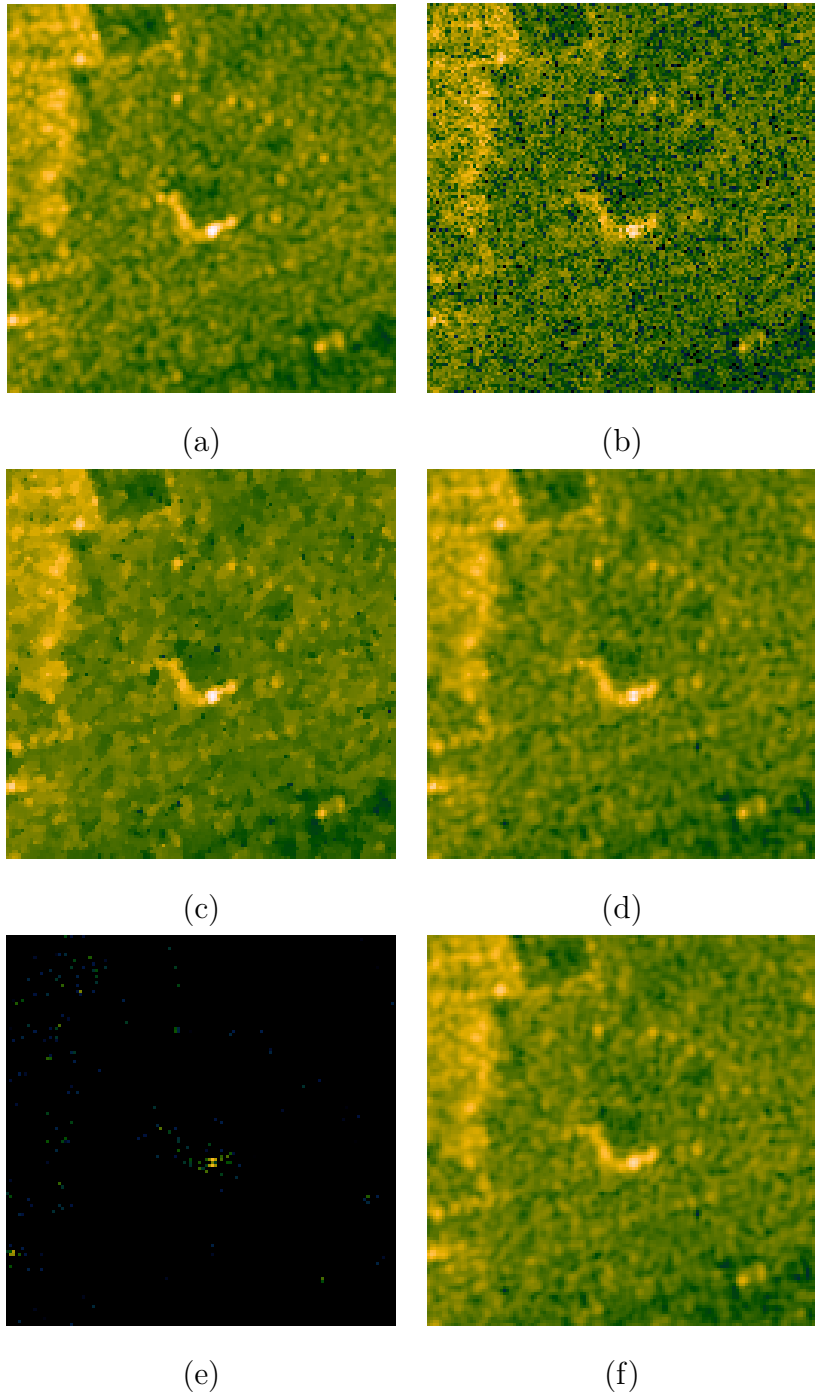


Figure 4.6: Result of the third experiment with $L \approx 0.71$. (a) Reconstructed image with full data. (b) Conventional reconstruction. (c) Image reconstructed with point-region enhanced regularization. (d) Proposed method: Composite image. (e) Proposed method: sparse image. (f) Proposed method: low-rank image.

Chapter 5

Conclusion and Future Work

5.1 Conclusion

In this thesis, we have contributed the area of SAR image reconstruction. Firstly, we have incorporated learning-based dictionaries into the sparsity-driven SAR imaging problem. Our approach can learn dictionaries from a training set of images offline, or from the data to be used in image reconstruction online. Experimental results have shown that learning-based approaches can widen the domain of applicability of sparsity-driven SAR imaging, and enable exploitation of context-based knowledge for more effective sparse representation in SAR. Secondly, we have proposed low-rank sparse decomposition (LRSD) based SAR image reconstruction framework. The proposed method reconstructs the SAR image while decomposing the sparse and the low-rank background part of the SAR image.

In Chapter 3 we have presented the mathematical formulation of our dictionary learning-based framework. Our sparsity-driven framework consists of a data term and a prior term. We have used a prior term that is sparsity-based on a learned dictionary. Our framework is adaptive to the reflectivity field so it can represent wide set of images sparsely. We have proposed an iterative method for the solution of the optimization problem posed in our framework by using a coordinate descent method. We have provided both synthetic and real SAR image experiments. In synthetic image experiments, we have compare our online and offline learning-based approaches with the conventional reconstruction method, point-region enhanced non-quadratic regularization, as well as

sparsity-driven SAR imaging with predefined dictionaries. We present the performance of these methods with respect to number of available data and noise. Our experiments have shown that, our online and offline dictionary learning-based approaches provides more accurate reconstructions. We have also presented visual experiment results for qualitative comparison. We have seen that, our approach can preserve patterns and features in the image because of its adaptivity.

In Chapter 4 we have proposed a framework for SAR image formation based on a low-rank and sparse decomposition of the scene to be imaged. Most of the imaging applications involving SAR images require background subtraction or segmentation for better interpretation of the image. Thus, we have proposed a SAR image reconstruction framework that separates background from sparse regions while reconstructing the SAR image. We have shown that this approach provides accurate reconstruction performance as compared to the existing reconstruction methods. Moreover, separating background from sparse regions may facilitate further SAR image analysis.

5.2 Potential Future Directions

There are several potential future directions for our research. In Chapter 3 we proposed SAR image reconstruction method that is based on adaptively learned dictionaries. An alternative for this framework is using combined dictionaries. In particular, a dictionary may consist of fixed atoms and adaptive atoms. We mentioned that the performance of the online learning approach deteriorates when the number of data samples data is low. Thus, fixed atoms may improve the reconstruction performance for the first iterations in such settings and for the later iterations online learning may be more effective.

We have used a relatively simple method for phase estimation in our approach. As a prior term we have exploited the fact that the magnitude of exponentiated phase is unity. However, even though the phase of the complex-valued SAR images is usually highly random, there might be some features within the phase that is to be learned. These features can be adapted to phase estimation framework. Besides, probabilistic

approaches can also be used by enforcing uniformly distributed phase.

We have separated the reconstruction of the magnitude and the phase of SAR image in our framework. Thus, we enforce sparsity on the magnitude of the SAR image. This situation poses an additional constraint that the solution should be non-negative. We have not used non-negativity constraints in our framework due to the additional computational burden that would be caused by the extra constraint. However, in future work this constraint can be used for better performance.

In Chapter 4 we enforce sparsity on the SAR image directly. An alternative approach can be using sparsifying transform (dictionary) for better sparse representation. Moreover, proposed LRSD-based SAR image reconstruction framework can be used for further SAR imaging applications such as wide-angle, and moving target imaging.

Bibliography

- [1] V. Abolghasemi and L. Gan, “Dictionary learning for incomplete SAR data,” in *International Workshop on Compressed Sensing Applied to Radar*, 2012.
- [2] M. Aharon, “Overcomplete dictionaries for sparse representation of signals,” *PhD Thesis, The TechnionIsrael Institute of Technology*, 2006.
- [3] M. Aharon, M. Elad, and A. Bruckstein, “K -SVD: An algorithm for designing overcomplete dictionaries for sparse representation,” *IEEE Transactions on Signal Processing*, vol. 54, no. 11, pp. 4311–4322, Nov 2006.
- [4] Astrium TerraSAR-X sample imagery. [Online]. Available: <http://www.astriumgeo.com/en/23-sample-imagery>
- [5] S. Boyd, N. Parikh, E. Chu, B. Peleato, and J. Eckstein, “Distributed optimization and statistical learning via the alternating direction method of multipliers,” *Found. Trends Mach. Learn.*, vol. 3, no. 1, pp. 1–122, Jan. 2011.
- [6] A. Bruckstein, M. Elad, and M. Zibulevsky, “On the uniqueness of nonnegative sparse solutions to underdetermined systems of equations,” *IEEE Transactions on Information Theory*, vol. 54, no. 11, pp. 4813–4820, Nov 2008.
- [7] T. B. C. Guyon and E. Zahzah, *Robust Principal Component Analysis for Background Subtraction: Systematic Evaluation and Comparative Analysis*. INTECH, 1995.
- [8] J.-F. Cai, E. J. Candes, and Z. Shen, “A Singular Value Thresholding Algorithm for Matrix Completion,” *ArXiv e-prints*, Oct. 2008.

- [9] E. J. Candès, X. Li, Y. Ma, and J. Wright, “Robust principal component analysis?” *J. ACM*, vol. 58, no. 3, pp. 11:1–11:37, Jun. 2011.
- [10] E. J. Candes, J. K. Romberg, and T. Tao, “Stable signal recovery from incomplete and inaccurate measurements,” *Communications on Pure and Applied Mathematics*, vol. 59, no. 8, pp. 1207–1223, 2006.
- [11] E. Cands and B. Recht, “Exact matrix completion via convex optimization,” *Foundations of Computational Mathematics*, vol. 9, no. 6, pp. 717–772, 2009.
- [12] W. Carrara, R. Majewski, and R. Goodman, *Spotlight Synthetic Aperture Radar: Signal Processing Algorithms*. Artech House, 1995.
- [13] M. Çetin, “Feature-enhanced synthetic aperture radar imaging,” *PhD Thesis, Boston University*, 2001.
- [14] M. Çetin and W. C. Karl, “Feature-enhanced synthetic aperture radar image formation based on nonquadratic regularization,” *IEEE Trans. Image Processing*, pp. 623–631, 2001.
- [15] M. Cetin, I. Stojanovic, N. Onhon, K. Varshney, S. Samadi, W. Karl, and A. Will-sky, “Sparsity-driven synthetic aperture radar imaging: Reconstruction, autofocus-ing, moving targets, and compressed sensing,” *IEEE Signal Processing Magazine*, vol. 31, no. 4, pp. 27–40, July 2014.
- [16] C.-F. Chen, C.-P. Wei, and Y.-C. Wang, “Low-rank matrix recovery with struc-tural incoherence for robust face recognition,” in *Computer Vision and Pattern Recognition (CVPR), 2012 IEEE Conference on*, June 2012, pp. 2618–2625.
- [17] S. S. Chen, D. L. Donoho, Michael, and A. Saunders, “Atomic decomposition by basis pursuit,” *SIAM Journal on Scientific Computing*, vol. 20, pp. 33–61, 1998.
- [18] M. Dao, L. H. Nguyen, and T. D. Tran, “Temporal rate up-conversion of synthetic aperture radar via low-rank matrix recovery,” in *IEEE International Conference on Image Processing, ICIP 2013, Melbourne, Australia, September 15-18, 2013*. IEEE, 2013, pp. 2358–2362.

- [19] L. Denis, F. Tupin, J. Darbon, and M. Sigelle, “SAR image regularization with fast approximate discrete minimization,” *IEEE Transactions on Image Processing*, vol. 18, no. 7, pp. 1588–1600, July 2009.
- [20] W. Dong, D. Zhang, G. Shi, and X. Wu, “Image deblurring and super-resolution by adaptive sparse domain selection and adaptive regularization,” *IEEE Transactions on Image Processing*, vol. 20, no. 7, pp. 1838–1857, July 2011.
- [21] D. L. Donoho, “Compressed sensing,” *IEEE Trans. Inform. Theory*, vol. 52, no. 4, pp. 1289 – 1306, 2006.
- [22] M. Elad and M. Aharon, “Image denoising via sparse and redundant representations over learned dictionaries,” *IEEE Transactions on Image Processing*, vol. 15, no. 12, pp. 3736–3745, Dec 2006.
- [23] K. Engan, S. O. Aase, and J. H. Husøy, “Multi-frame compression: Theory and design,” *Signal Process.*, vol. 80, no. 10, pp. 2121–2140, Oct. 2000.
- [24] D. Gabay and B. Mercier, “A dual algorithm for the solution of nonlinear variational problems via finite element approximation,” *Computers & Mathematics with Applications*, vol. 2, no. 1, pp. 17 – 40, 1976.
- [25] C. Gao, D. Meng, Y. Yang, Y. Wang, X. Zhou, and A. Hauptmann, “Infrared patch-image model for small target detection in a single image,” *IEEE Transactions on Image Processing*, vol. 22, no. 12, pp. 4996–5009, Dec 2013.
- [26] A. Gersho and R. M. Gray, *Vector Quantization and Signal Compression*. Norwell, MA, USA: Kluwer Academic Publishers, 1991.
- [27] I. Gorodnitsky and B. Rao, “Sparse signal reconstruction from limited data using focuss: a re-weighted minimum norm algorithm,” *IEEE Transactions on Signal Processing*, vol. 45, no. 3, pp. 600–616, Mar 1997.
- [28] C. He, L. Liu, L. Xu, M. Liu, and M. Liao, “Learning based compressed sensing for SAR image super-resolution,” *IEEE Journal of Selected Topics in Applied Earth Observations and Remote Sensing*, vol. 5, no. 4, pp. 1272–1281, 2012.

- [29] M. Hestenes, “Multiplier and gradient methods,” *Journal of Optimization Theory and Applications*, vol. 4, no. 5, pp. 303–320, 1969.
- [30] P. Hoyer, “Non-negative sparse coding,” in *Neural Networks for Signal Processing, 2002. Proceedings of the 2002 12th IEEE Workshop on*, 2002, pp. 557–565.
- [31] J. Jiang, L. Jiang, and N. Sang, “Non-local sparse models for SAR image despeckling,” in *International Conference Computer Vision in Remote Sensing (CVRS)*, 2012, pp. 230–236.
- [32] M. S. Lewicki and B. A. Olshausen, “Probabilistic framework for the adaptation and comparison of image codes,” *J. Opt. Soc. Am. A*, vol. 16, no. 7, pp. 1587–1601, Jul 1999.
- [33] M. S. Lewicki and T. J. Sejnowski, “Learning overcomplete representations,” *Neural Comput.*, vol. 12, no. 2, pp. 337–365, Feb. 2000.
- [34] Z. Lin, M. Chen, and Y. Ma, “The Augmented Lagrange Multiplier Method for Exact Recovery of Corrupted Low-Rank Matrices,” *ArXiv e-prints*, Sep. 2010.
- [35] S. Lingala, Y. Hu, E. DiBella, and M. Jacob, “Accelerated dynamic MRI exploiting sparsity and low-rank structure: k-t SLR,” *IEEE Transactions on Medical Imaging*, vol. 30, no. 5, pp. 1042–1054, May 2011.
- [36] S. Ma, D. Goldfarb, and L. Chen, “Fixed point and bregman iterative methods for matrix rank minimization,” *Math. Program.*, vol. 128, no. 1-2, pp. 321–353, Jun. 2011.
- [37] J. Mairal, M. Elad, and G. Sapiro, “Sparse representation for color image restoration,” *IEEE Transactions on Image Processing*, vol. 17, no. 1, pp. 53–69, Jan 2008.
- [38] S. Mallat and Z. Zhang, “Matching pursuits with time-frequency dictionaries,” *IEEE Transactions on Signal Processing*, vol. 41, no. 12, pp. 3397–3415, Dec 1993.

- [39] D. C. Munson, Jr., J. D. O'Brien, and W. K. Jenkins, "A tomographic formulation of spotlight-mode synthetic aperture radar," *Proc. IEEE*, vol. PROC-71, pp. 917–925, 1983.
- [40] Y. C. Pati, R. Rezaifar, Y. C. P. R. Rezaifar, and P. S. Krishnaprasad, "Orthogonal matching pursuit: Recursive function approximation with applications to wavelet decomposition," in *Proceedings of the 27th Annual Asilomar Conference on Signals, Systems, and Computers*, 1993, pp. 40–44.
- [41] D. L. Phillips, "A technique for the numerical solution of certain integral equations of the first kind," *J. ACM*, vol. 9, no. 1, pp. 84–97, Jan. 1962.
- [42] L. Potter, E. Ertin, J. Parker, and M. Cetin, "Sparsity and compressed sensing in radar imaging," *Proceedings of the IEEE*, vol. 98, no. 6, pp. 1006–1020, June 2010.
- [43] L. C. Potter, P. Schniter, and J. Ziniel, "Sparse reconstruction for radar," *Proc. SPIE*, vol. 6970, pp. 697 003–697 003–15, 2008.
- [44] W. Rao, G. Li, X. Wang, and X.-G. Xia, "Adaptive sparse recovery by parametric weighted l_1 minimization for isar imaging of uniformly rotating targets," *IEEE Journal of Selected Topics in Applied Earth Observations and Remote Sensing*, vol. 6, no. 2, pp. 942–952, April 2013.
- [45] S. Ravishankar and Y. Bresler, "MR image reconstruction from highly undersampled k-space data by dictionary learning," *IEEE Trans. Medical Imaging*, vol. 30, no. 5, pp. 1028–1041, 2011.
- [46] B. Recht, M. Fazel, and P. Parrilo, "Guaranteed minimum-rank solutions of linear matrix equations via nuclear norm minimization," *SIAM Review*, vol. 52, no. 3, pp. 471–501, 2010.
- [47] R. Rubinstein, A. Bruckstein, and M. Elad, "Dictionaries for sparse representation modeling," *Proceedings of the IEEE*, vol. 98, no. 6, pp. 1045–1057, June 2010.
- [48] L. I. Rudin, S. Osher, and E. Fatemi, "Nonlinear total variation based noise removal algorithms," *Phys. D*, vol. 60, no. 1-4, pp. 259–268, Nov. 1992.

- [49] S. Samadi, M. Cetin, and M. Masnadi-Shirazi, “Sparse representation-based synthetic aperture radar imaging,” *IET Radar, Sonar and Navigation*, vol. 5, no. 2, pp. 182–193, 2011.
- [50] S. Samadi, M. Cetin, and M. Masnadi-shirazi, “Multiple feature-enhanced SAR imaging using sparsity in combined dictionaries,” *IEEE Geoscience and Remote Sensing Letters*, vol. 10, no. 4, pp. 821–825, July 2013.
- [51] C. W. Sherwin, J. P. Ruina, and R. D. Rawcliffe, “Some early developments in synthetic aperture radar systems,” *IRE Transactions on Military Electronics*, vol. MIL-6, no. 2, pp. 111–115, April 1962.
- [52] J.-L. Starck, M. Elad, and D. Donoho, “Image decomposition via the combination of sparse representations and a variational approach,” *IEEE Transactions on Image Processing*, vol. 14, no. 10, pp. 1570–1582, Oct 2005.
- [53] I. Stojanovic, “Sparse reconstruction in monostatic and multistatic SAR,” *Boston University*, 2012.
- [54] M. Tao and X. Yuan, “Recovering low-rank and sparse components of matrices from incomplete and noisy observations,” *SIAM J. on Optimization*, vol. 21, no. 1, pp. 57–81, Jan. 2011.
- [55] R. Tibshirani, “Regression shrinkage and selection via the lasso,” *Journal of the Royal Statistical Society, Series B*, vol. 58, pp. 267–288, 1994.
- [56] A. N. Tikhonov, “Solution of incorrectly formulated problems and the regularization method,” *Soviet Math. Dokl.*, vol. 4, pp. 1035–1038, 1963.
- [57] K. C. Toh, M. Todd, and R. H. Ttnc, “SDPT3 – a MATLAB software package for semidefinite programming,” *OPTIMIZATION METHODS AND SOFTWARE*, vol. 11, pp. 545–581, 1999.
- [58] B. Tremoulheac, N. Dikaios, D. Atkinson, and S. Arridge, “Dynamic MR image reconstructionseparation from undersampled (\mathbf{k}, t) -space via low-rank plus sparse

- prior,” *IEEE Transactions on Medical Imaging*, vol. 33, no. 8, pp. 1689–1701, Aug 2014.
- [59] C. Vogel and M. Oman, “Fast, robust total variation-based reconstruction of noisy, blurred images,” *IEEE Transactions on Image Processing*, vol. 7, no. 6, pp. 813–824, Jun 1998.
- [60] J. X. Yuan, “Sparse and Low-Rank Matrix Decomposition Via Alternating Direction Methods,” *Optimization Online*, 2009.
- [61] G. Xu, M. Xing, L. Zhang, Y. Liu, and Y. Li, “Bayesian inverse synthetic aperture radar imaging,” *IEEE Geoscience and Remote Sensing Letters*, vol. 8, no. 6, pp. 1150–1154, Nov 2011.
- [62] Q. Xu, H. Yu, X. Mou, L. Zhang, J. Hsieh, and G. Wang, “Low-dose x-ray ct reconstruction via dictionary learning,” *IEEE Transactions on Medical Imaging*, vol. 31, no. 9, pp. 1682–1697, Sept 2012.
- [63] D. Yang, G. Liao, S. Zhu, X. Yang, and X. Zhang, “Sar imaging with undersampled data via matrix completion,” *IEEE Geoscience and Remote Sensing Letters*, vol. 11, no. 9, pp. 1539–1543, Sept 2014.
- [64] X. X. Zhu and R. Bamler, “Tomographic sar inversion by l_1 -norm regularization; the compressive sensing approach,” *IEEE Transactions on Geoscience and Remote Sensing*, vol. 48, no. 10, pp. 3839–3846, Oct 2010.